Dynamic tensile behaviours of heterogeneous rocks: the grain scale fracturing characteristics on strength and fragmentation

X.F. Li , X. Li , H.B. Li , Q.B. Zhang , J. Zhao

PII: S0734-743X(17)31055-2
DOI: 10.1016/j.ijimpeng.2018.04.006
Reference: IE 3091

To appear in: *International Journal of Impact Engineering*

Received date: 4 December 2017
Revised date: 30 March 2018
Accepted date: 7 April 2018

Please cite this article as: X.F. Li , X. Li , H.B. Li , Q.B. Zhang , J. Zhao , Dynamic tensile behaviours of heterogeneous rocks: the grain scale fracturing characteristics on strength and fragmentation , *International Journal of Impact Engineering* (2018), doi: 10.1016/j.ijimpeng.2018.04.006

Highlights

- Grain scale discrete element model is proposed to study dynamic properties of rocks.
- Heterogeneous rocks are reproduced and micro fracturing characteristics are investigated.
- Rocks behave fragmentation transition from sparse fracture to pervasive pulverization as the strain rate increased.
- Strain rate mechanism is related to micro fracturing transition from intergranular to transgranular.

Dynamic tensile behaviours of heterogeneous rocks: the grain scale fracturing characteristics on strength and fragmentation

List of authors:

Dr. X.F. Li (First author)
xfli@whrsm.ac.cn
State Key Laboratory of Geomechanics and Geotechnical Engineering, Institute of Rock and Soil Mechanics, Chinese Academy of Sciences, Wuhan 430071, China
University of Chinese Academy of Sciences, Beijing 10049, China
Department of Civil Engineering, Monash University, Clayton, VIC 3800, Australia

Associate Prof. X. Li (Corresponding author)
li.xing@outlook.com
Department of Civil Engineering, Monash University, Clayton, VIC 3800, Australia
School of Civil Engineering, Southeast University, Nanjing, Jiangsu 211189, China

Prof. H.B. Li
hbli@whrsm.ac.cn
State Key Laboratory of Geomechanics and Geotechnical Engineering, Institute of Rock and Soil Mechanics, Chinese Academy of Sciences, Wuhan 430071, China

Dr. Q.B. Zhang
qianbing.zhang@monash.edu
Department of Civil Engineering, Monash University, Clayton, VIC 3800, Australia

Prof. J. Zhao
jian.zhao@monash.edu
Department of Civil Engineering, Monash University, Clayton, VIC 3800, Australia

Abstract: The dynamic tension behaviours of granites are tested with the split Hopkinson pressure bar and the quasi-static responses including the compression and Brazilian splitting are carried out with a material testing system. The experimental results show the tensile strengths behave significant strain rate effect. In order to characterize the realistic fracturing process from the viewpoint of grain scale failure, a multiple scale discrete element model considering the micro heterogeneity is proposed using the digital image processing of mineral scanning for rocks. Comparison of the experimental and numerical tension stress as well as the ultimate fragment state indicates the grain-based model is reasonable in simulation of dynamic tension test on granites. Then the three-wave superposition, crack propagation sequences, end forces and the stress distribution are discussed to confirm the stress equilibrium in the specimen. Using the micro heterogeneous model, the micro fracturing process and fragmentation in association with energy dissipation at different strain rates are discussed. It is found that the failure sequence can be divided into five stages as crack initiation, propagation, coalesce, branching and indentation crush on the stress curve in dynamic loading. The intrinsic mechanism of the strain rate effect is believed to be the transitions of the micro fracturing type, orientation and the damage degree in the specimen and in turn exhibiting more energy dissipation as well as fragmentation transition from sparse fracture to pervasive pulverization. Finally, the scaling model of the dynamic increase factor for granite is derived and the characteristic strain rate, increase rate factor values are discussed.

Key words: Strain rate effect, dynamic tensile strength, granular rocks, DEM simulation, micro fracturing

1. Introduction

Understanding dynamic behaviours of rocks is of significance in many areas such as rock breakage (*Grady, 1982*), blasting (*Grady and Kipp, 1980*), planetary collision (*Hogan et al., 2015*) and prevention from projectile impact (*Schultz et al., 2007*). Recent research on mechanical properties of rocks manifest the brittle materials will experience strong rate sensitivity in rupturing strength once the dynamic fracturing of pre-existed defects is mobilized (*Zhang and Zhao, 2014, Aben et al., 2016*). The initiation, propagation and coalesce of internal flaws are associated with huge amount of energy dissipation and result in fragmentation transition from sparse fracture to pervasive pulverization which rarely observed in quasi-static experiments (*Yuan et al., 2011*). These pulverized fragments performed from the crystal grain to the original rock fabric at different scales and ultimately leaded to complicated dynamic fracturing features (*Hong et al. 2009*). Among these, the tensile behaviour is recognized as an important role determining dynamic properties of rocks as well as debris formation during the failure processing. In the past decades, studies on the tensile behaviours of rocks under dynamic loads have received significant attentions from experimental viewpoint. For example, *Asprone et al. (2009)* and *Cadoni (2010)* explored the dynamic tensile strength of two rocks (e.g. Naples tuff, Onsernone Orthogneiss) by using the direct tension (DT) test on the split Hopkinson bar (Kolsky bar). To minimize stress concentrations at the ends of the sample, a new configuration of bone-shaped (*Howe et al., 1974; Goldsmith et al., 1976*) and dumbbell-shaped (*Huang et al., 2010*) specimens was used. Besides, the dynamic indirect tension test on rock materials including Brazilian disc (BD) method (*Gomez et al., 2001; Cai et al., 2007; Dai et al., 2010; Zhang and Zhao, 2013*), flatted Brazilian disc (FBD) method (*Wang et al, 2006; Wang et al, 2009; Yu et al, 2009*), Brazilian jaw (BJ) method (*Dai et al., 2010a*), semi-circular bending (SCB) bending method (*Dai et al, 2008; Dai et al, 2010a; Dai et al, 2010b*), spherical ball method (*Huang et al, 2014a*) and spalling method (*Khan and Irani, 1987; Kubota et al., 2008; Johnson, 2010*) was widely performed due to the convenience for instrumentation and samples preparing. These studies emphasis on phenomenological descriptions of strain rate effects in rock strengths and overlook the heterogeneities of material on microstructures

fracturing and failure. There are although several theoretical studies including the thermal activation theory (*Kumar. 1968*) and the sliding crack theory (*Bhat et al., 2012*) having been attempted to link the dynamic behaviours to fracturing propagation. These models can be well used to present macroscopic rate dependency on failure strength as well as failure patterns after the dynamic loading, but still failed to explain the microscopic fracturing behaviours and catastrophic fragmentation at high strain rates, especially from the viewpoint of grain scale which ranges from 10^{-3} m to 10^{-4} m.

Numerical method is an alternative approach to overcome uncertain issues encountered in dynamic tests due to the advantages as: (a) the disturbances such as the ends friction, wave dispersion and stress equilibrium can be eliminated, (b) identical samples ensure the repeatability of simulated results, and (c) the internal variables such as damage evolution and energy dissipation are accessible to be directly measured. Common techniques used for rock tensile fracturing are finite element method (FEM) (*Cho et al., 2003; Saksala et al., 2015; Fang and Xu, 2016*), discrete element method (DEM) (*Xu et al., 2016*), finite-discrete element method (FEM/DEM) (*Mahabadi et al., 2010; Saksala et al., 2013; Rougier et al., 2014*), lattice spring model (*Zhao et al., 2014*), dual-horizon peridynamics (DH-PD) (*Rabczuk and Ren, 2017*), meshfree method (*Rabczuk and Belytschko, 2004*) and Voronoi-based discrete element method (*Gui et al., 2015*). During these methods, the DEM models the cracks as virtual discontinuities which are pre-existed in the medium and allows blocks separating on the cracks, which has been used to simulate the brittle fracturing and failure of rocks (*Farahmand et al., 2018*). In general, these methods simulate mechanical behaviours and failure for rocks at macro scope and the presences of grain scale microstructures are ignored.

At the grain scale, rock materials are heterogeneous and are composed of different mineral grains, each with varying geometry heterogeneity (e.g., grain size, shape and distribution) and mechanical heterogeneity (e.g., strength, moduli and fracture toughness). The heterogeneity of grain structures results in local concentration of tensile stress and in turn dominates the fracture mechanism for quasi-brittle materials. Especially in dynamic tests, the inertia of the micro crack propagation, the transition of fracturing paths and the grain scale pulverization

comprehensively influence the rate dependency for rocks. With a focus on the microstructure, few studies directly model rocks at grain scale and investigate microfracture initiation, propagation and coalescence. For example, *Zhao et al (2014)* combined the X-ray micro computed tomography with the DLSM and studied the influence of microstructures on the rate dependency of dynamic Brazilian disc test for sandstone. *Gui et al (2016)* used a mixed-mode cohesive fracture model accounting for the micro fracturing on the mineral grain boundaries to reproduce the dynamic tensile failure of rocks. The grain geometry is simulated as polygonal tessellations based on a stochastic distribution and therefore the simulated results are highly dependent on the distribution parameters. Another approach is to realistically reproduce the mineral structures in association with digital image technique (*Yue et al., 2003; Tan et al., 2016; Li et al., 2018*). The images of microstructures are carried out by the polarized microscope and the actual mineral grains geometry information (e.g. position, shape and size) is extracted after the image processing. Different from the continuum model (*Yue et al., 2003*) and partial discrete model (*Tan et al., 2016*), the novel model proposed in this study not only can simulate the realistic microstructures of samples but also reproduce the fracturing through the mineral grains.

In the present study, the experiments including the dynamic and quasi-static tests are carried out in granites for verifying numerical results. The grain-based DEM considering the actual heterogeneity of granular rocks is established using the digital image processing of mineral scanning images. Numerical dynamic tension test under a strain rate range of (5.7~41/s) are performed on granites. The simulated results are compared with the experiments and the stress equilibrium prerequisite is checked according to the stress state in the specimen. The micro fracturing sequence is discussed at different stress states and the dissipated energy, the micro fracturing distribution and the fragment size are computed to investigate the intrinsic mechanism of the strain rate effect for rocks. Finally, a unified scaling law of the dynamic increase factor is established and the characteristic strain rate as well as the increase rate factor is investigated.

2. Experimental set-up and results

2.1 Rock materials

In order to decrease the pre-existing cracks presence of the studied material, the medium-grained granite with low porosity (0.82 %) and water content is chosen for this research (see Fig. 1a). The average density was about 2.71 g/cm^3 and the P-wave velocity was 5421 m/s. Polarized microscope images indicate the granite sample is mainly composed of three kinds of mineral: feldspar, quartz and biotite (Fig. 1c-d). The corresponding volume ratios estimated by thin section analysis (listed in Table 1) are 26.3% (quartz), 51.7% (feldspar), 19.5% (biotite) and 2.5% (others). The grain size distributions are approximately isotropic and seriate, with average grain sizes from 0.95 to 2.38 mm for different minerals (in Fig. 1b). The grain size ratio $d_{\max}/d_{\min}$ is used to characterize the geometry heterogeneity induced by the microstructures. As shown in Table 1, the feldspar has the biggest grain size ratio $d_{\max}/d_{\min}$=5.4 and the following quartz is 3.2. The biotite has the lowest variance with a value of 2.6.

2.2 Static tensile tests with servo-hydraulic testing machine

An electro-hydraulic servo-operated material testing system using constant axial displacement controlling was performed for the uniaxial compression test of granites. The cylindrical specimen has a length of 100 mm and diameter of 50 mm following the ISRM recommendation. The applied strain rate was 5×10^{-5} /s to ensure the sample deformation in quasi-static state. The experimental results indicate that the elastic modulus of this granite was 42.3 GPa and the Poisson's ratio was 0.21. The average uniaxial compression strength was 129.6 MPa. The indirect tension test by Brazilian disc was carried out for the static tension strength. The dimensions of the Brazilian disc samples were 50 mm in diameter and 20 mm in thick as recommended by ISRM. The granite discs were compressed diametrically at a constant strain rate 1×10^{-5} /s by the flatten platen without any bearing strips or jaws. The quasi-static indirect tension strength of this granite was approximately 13.3 MPa.

2.3 Dynamic tensile tests with SHPB apparatus

The dynamic tension tests were carried out by the SHPB apparatus, which consists of five general parts: a striker, an incident bar, a transmitted bar, a damping configuration and the sample sandwiched in the incident bar and transmitted bar as shown in Fig. 2. In order to eliminate the wave disturbance reflected from the free boundary, the incident bar and the transmitted bar have the same length of 2.5 m. The diameter of the bars used in this study is 50 mm. The striker is shaped in the form of bullet and the length is 0.4 m. The brass pulse shaper having a diameter of 20 mm and thick of 2 mm was used to shape the loading pulse. The test samples, 50 mm in diameter and 15 mm in thick, were sandwiched in the incident bar and the transmitted bar without any bearing strips or jaws. In order to capture the tensile stress evolution in the sample, three strain gauges were mounted on the axial paralleling to the loading direction. The striker impacts the free end of the incident bar and generates a compressional wave $\varepsilon_{in}(t)$ towards to the sample. When the incident wave reached the interface between the sample and the incident bar, part of the wave is reflected as the reflected wave $\varepsilon_{re}(t)$ and the remaining wave continually propagates towards the transmitted bar as the transmitted wave $\varepsilon_{tr}(t)$. Therefore, the forces $P_1(t), P_2(t)$ at the ends of the specimen can be computed as

$$P_1(t) = E_b A_b [\varepsilon_{in}(t) + \varepsilon_{re}(t)] \tag{1}$$

$$P_2(t) = EA\varepsilon_{tr}(t) \tag{2}$$

where E_b and A_b are the elastic modulus and the cross-sectional area of the bars, respectively. When the stress equilibrium in the sample is ensured, the end forces satisfy $P_1(t) = P_2(t)$. The indirect tensile strength can be obtained as

$$\sigma_t = \frac{2P(t)_{\max}}{\pi d_s b_s} \tag{3}$$

where d_s and b_s are the diameter and thickness of the Brazilian disc sample and the force is $P(t) = [P_1(t) + P_2(t)]/2$. The loading rate can be determined by

$$\dot{\sigma}_t = \frac{\sigma_t}{t_p} \tag{4}$$

where σ_t is the indirect tensile strength and t_p is the corresponding time at the peak force $P(t)_{\max}$. Similarly, the strain rate $\dot{\varepsilon}_t$ can be computed as

$$\dot{\varepsilon}_t = \frac{\dot{\sigma}_t}{E_s} \tag{5}$$

where E_s is the elastic modulus of the sample.

2.4 Dynamic behaviours of granular rock

The prerequisites of the SHPB technique for rock tension testing are the stress equilibrium in sample and crack initiation from the disc center. According to the stress responses of the sample, the dynamic tension behaviours induced by SHPB can be categorized into two types as shown in Fig 3-4. The recorded strain signals from the incident/transmitted bars when the strain rate $\dot{\varepsilon}$ =7.2 /s are shown in Fig. 3a. The incident wave is approximately semisinusoidal after the attenuation of high-frequency components by the brass pulse shaper. The signals from strain gauges mounted on the sample surface indicate the crack initiated from the SG.1 at t=780 μs. This fracture propagates to SG.2 or SG.3 at t=792 μs and therefore the corresponding cracking velocity is about 1041 m/s. The coincidence of the SG. 2 and SG.3 fracturing time reveals that the stress equilibrium in the sample is well ensured. This result also can be drawn from the three-wave equilibrium as shown in Fig. 3b, due to the fact that the superposition of the two ends force (In.-Tr.+Re.) is restricted to the range below 5% of the peak transmitted strain. Directly measuring the forces at the ends of the specimen is carried out to evaluate the equilibrium duration during the loading process as shown in Fig.3c. The stress equilibrium factor $\eta = {2(P_1 - P_2)}/{(P_1 + P_2)}$ is used herein to represent the equilibrium state in the sample. It is found that the equilibrium begins at t=53 μs and ends up at t=101 μs after the peak failure. This equilibrium stage covers the elastic loading processing until to the dominant fracturing at the peak point. The indirect failure strength is 23.2 MPa with a corresponding duration $\tau = 42$ μs as shown in Fig.3d. The loading rate is about 303 GPa/s and the strain rate computed by Eq.5 is 7.2 /s. The fracturing characteristic shows that the fracturing surface is parallel to the loading direction at the disc center without ends indentation failure.

Fig. 4 is the comparing results of Fig.3 when the strain rate is 14 /s. Several interesting conclusions can be observed: (a) the crack propagation from the SG.1, SG.2 and SG.3 was no more sequential. SG.3 is increased more dramatically at the beginning loading due to the

inertia stress preceding the equilibrium. This behaviour results in macro crack fracturing from the incident end to the transmitted end. (b) although the three-wave equilibrium shows available agreement in Fig. 4b, the equilibrium stage is decreased to t =61~77 μs . In particular at the moment of the peak failure, the specimen has lost the assumption of stress equilibrium. (c) the roughly nonequilibrium loading results in fragments of the specimen, including the indentation at the loading points and the branching at the disc center. The failure strength is as high as 37.3 MPa and the loading rate is almost 594 GPa/s with a corresponding strain rate of 14 /s. (d) the platform resulted from the inertia impacting of fractured specimen is easily observed from the transmitted gauge.

3. Grain-based discrete element method

The discrete element method (DEM) allowing the breakage or separation between basic elements has advantages of reproducing the realistic failure process of the rock materials. With the introduction of the particle-based DEM by *Cundall and Strack (1979)*, the uncertainties regarding the contact detection in block-based DEM was improved and in turn promoting the popularization of using DEM for geomaterials. In granular medium, the distinct particles are bonded by pre-existed contacts regardless of obeying deformation compatibility. These contacts will be ruptured when the tensile/shear stress exceeds the failure limitation. Considering the computation efficiency, these particles are commonly modelled at millimeter scale which is characterized by the mineral grains observed in laboratory. The coarse grain boundaries and the fracturing through the grains cause inconsistency with the rigid circular particles assumption in particle-based DEM. The grain-based DEM (GB-DEM) aimed to characterize the realistic grain scale behaviours such as the material heterogeneity, mineral grains deformation and grain fracturing for rocks is presented in this section.

3.1 GB-DEM modelling on rock heterogeneity

Rock heterogeneity modelling has been extensively performed by continuum method (*Li et al, 2003; Farahmand and Diederichs, 2016)*, block-based DEM (*Lan et.al, 2010; Tan, 2016; Li et al, 2016*), particle-based DEM (*Bahrani et al, 2014; Bahrani and Kaiser, 2017*), etc.. In the continuum context, the material heterogeneity is revealed by the

localization of meshes regardless of realistic fracturing along the boundary or intra the grains. The Voronoi tessellation used in block-based DEM treated the grain boundaries as discontinuities existed in nature and the fracturing pattern is determined by the stress state adjacent to the polygonal blocks. The continuum algorithm within the grains limits the realistic reproducing of the transgranular fracturing. Unlike the block-based DEM, the particle-clustered grains have two-scale geometry characterization as shown in Fig. 5. The intergranular contacts are inherited from the algorithm presented in block-based DEM and the transgranular contacts are reproduced to inverse the behaviors of grain materials themselves. These grains clustered by distinct particles can be used to reveal the fracturing among grains as well as the intergranular rupturing.

The rock heterogeneity resulted from the mineral grains is commonly modelled through a stochastic distribution. This methology results in qualitative performance in macro because its dependency on the statistical distribution parameters. Realistic reproduction of the grain shape, distribution and area based on digital image processing is used in this study. Fig. 6 illustrated the flow chart of the grain-based model generation as follows: (1) Identification of grain compositions by grey level analysis based on the fact that different mineral compositions are distinguished by setting color thresholds. (2) Locating the grain shapes and positions by simplifying the mineral grains as convex polygon tessellations. (3) Import the geometry information including the grain category and geometry position into the particle-based model. (4) The homogenous particles are clustered as mineral grains by grouping the particles and assigning different micro parameters. To reduce the errors caused by the out-of-plane crystalline structure, the investigated plane by the thin section test is identical with the scanning plane modelled by GB-DEM. Besides, the scanning electron microscope images (three-dimensional) are used to compare with polarized microscope images for analyzing the influence of crystalline structures.

3.2 Principal of contact model

The GB-DEM is built on the interaction between the soft contact and the rigid particles. The explicit time integration of the Newton's equation provides the updated displacement and velocity for each particle. The complicated macro behaviours including the damage evolution,

post-peak rupturing and strain softening are dependent on the interaction between particles and the contact model. In comparing with the particle-based DEM, the grain heterogeneity is considered in geometry modelling and the contact model for description the grain boundary is improved. The physical models described in the specimen included two-scale structures: a). grain behaviours between different mineral grains as shown in Fig. 7b and b). particle behaviours intra the grains as shown in Fig. 7c. The grain movement is revealed by the assemble interaction of the composed particles as shown in Fig. 7a. The movement between two polygon grains is divided into opening/closure in the normal direction and sliding in the tangential direction of the contact. Therefore the failure type on the grain boundary includes the tensile fracturing and shear sliding (in Fig. 7b). In a similar way, the particle movement within the grains also contains the normal direction moving and the tangential direction moving (in Fig. 7c). The mechanical behavior of the contacts (either the intergranular contact or the transgranular contact) is determined by the Mohr-Coulomb friction law as shown in Fig. 8. In the normal direction, the stress-displacement is simplified as linear elastic-brittle which is governed by the normal stiffness k_n and the tensile strength σ_t

$$\sigma_n = \begin{cases} k_n u_n & \sigma_n \leq \sigma_t \\ 0 & \sigma_n > \sigma_t \end{cases} \tag{6}$$

where u_n is the displacement in the normal direction and σ_n is the corresponding normal stress. When the stress σ_n exceeds the tensile strength of the contact σ_t, this contact is ruptured by tension failure. The contact also undergoes unlimited compression when the overlap between two elements is less than the initial gap (in Fig. 8a).

Similarly, the tangential behaviour is determined by the Coulomb sliding which is computed in incremental form as (shown in Fig. 8b)

$$\Delta\tau = k_s \Delta u_s \tag{7}$$

where k_s is the shear stiffness of the contact and $\Delta\tau, \Delta u_s$ are the incremental shear stress and displacement components. The contact will rupture in shear failure when the cumulative shear stress exceeds the shear strength $\tau_{\max}$

$$\tau_{\max} = \begin{cases} c - \sigma_n \tan\phi & \sigma_n \leq 0 \\ c & \sigma_n > 0 \end{cases} \tag{8}$$

where c and ϕ are the cohesion and friction angle of the contact and σ_n is the compressional stress. After the bonded contact has been broken, the new generated contact

inherits the elastic properties of the original contact and only Coulomb sliding is allowed in the tangential direction as

$$\tau = \sigma_n \mu \tag{9}$$

where μ is the residual friction of the unbonded contact. As shown in Fig. 9, the intergranular contact (IG contact) and the transgranular contact (TG contact) are controlled by different mechanical properties. These parameters are calibrated by the mineral grain experiments.

4. Numerical modelling of SHPB testing on Brazilian specimens

The SHPB apparatus is modelled with identical geometry considering both the realistic configuration and computation efficiency. As shown in Fig. 10, the incident and transmitted bars have lengths of 1.5 m and 0.75 m, respectively. The bar diameter is corresponded to the experimental condition and the value is set as 50 mm in this research. In order to eliminate the wave dispersion induced by Poisson effect in the bars, the incident and transmitted bars are regularly assembled by same-diameter particles. The bar contacts are supposed to follow the linear elastic model and the micro parameters are listed in Table 2. The rock sample is modelled as a disc having a diameter of 25 mm, and the particle radius ranges from 0.08 mm to 0.13 mm with a Gauss distribution. The number of the particles in the rock sample is 68693, therefore the size effect on the numerical results can be overlooked. The mineral grains geometry is realistically mapped by the digital image processing and the grain number in the specimen is about 2052. The average grain diameter is 1.52 mm and the minimum particle radius is 0.08 mm. Internal to the grains are 46~73 particles for different mineral compositions. Therefore, the fractured contacts can be categorized into the tensile fracturing (IG: tension), the shear fracturing (IG: shear) on the grain boundaries and the tensile fracturing (TG: tension), the shear fracturing (TG: shear) in the grains as schematized in Fig. 9.

Moreover, two measurement circles are assigned at the middle of the incident and transmitted bars (point A and B in Fig. 10) to represent the strain gauges mounted on bars. The end forces are directly recorded in the simulation process and three strain gauges are assigned to monitor the crack sequences. In order to avoid the disturbance of the reflected wave from the free

boundaries, the non-reflection boundaries are added.

The micro properties of the GB-DEM contacts are calibrated from the behaviour of mineral material and the overall properties of the rocks, i.e. the strength (uniaxial compression strength, Brazilian tension strength) and elastic properties. This work has been discussed in Ref. *Li et al (2016)* and the suggestive micro parameters for the granite are listed in Table 3. To ensure that the numerical results are comparable with the experimental observations, the incident stress waves are derived from the experiments and directly applied at the free end of the incident bar as shown in Fig. 11a. The experimental and simulated tensile stresses and ultimate failure modes are compared in Fig. 11b-c. At lower strain rate presented in Test 1, the experimental and simulated failure modes both display the expected axial splitting along the loading direction as well as the crushed wedges beneath the loading points. The tensile stress is identical with testing results and no platform can be observed after the peak failure. The fragmentation degree is more significant when the loading strain rate is increased in Test 2. Large scale crushed wedges which resulted from shear fracturing are generated at the contact areas and fragments induced by branching cracks also occur at the center of the sample both in numerical and experimental observations. This failure will resulted in unequilibrium loading during the failure process and in turn perform a platform on the stress curves. These results indicate that this model is reasonable to characterize the realistic behaviours of granites under dynamic loading.

5. Simulation result and discussion

5.1 Stress equilibrium validity

The premise of constant strain rate loading is the specimen under an stress equilibrium state. Considering the significantly limited failure strain in tension test for brittle rocks, the pulse shaping technique was carried out to generate a less abruptly increasing stress wave in experiments as shown in Fig. 11a. In the case of simulated Test 1, the time-shifted incident, reflected and transmitted wave stresses are plotted in Fig. 12a. The superposed stress of the incident wave $\sigma_{inc.}$, reflected wave $\sigma_{ref.}$ and transmitted wave $\sigma_{tra.}$ is limited to the range of $0\sim0.05\sigma_{ref.}$.The strain signals in Fig. 12b presented the crack sequences of the specimen. The

middle strain gauge SG.1 ruptured at $t_1 \approx 80\ \mu s$, because the SG.1 was not exactly fractured by the dominant fracture in the ultimate state, the strain is released after a suddenly increase induced by the tensile fracturing. This fracture almost simultaneously reached the SG.2 and SG.3 at $t_2 \approx 91\ \mu s$. The distance between SG.1 and SG.2 is 12.5 mm and therefore the computed crack velocity is approximate 1136 m/s. Checking the stress equilibrium period when the crack propagation across the specimen presented in Fig. 12c, the end stresses σ_1 and σ_2 match well with each other with reasonable accuracy. A stress equilibrium factor ξ is defined herein to evaluate the equilibrium degree at the specimen ends as

$$\xi = \frac{1}{2}\frac{\sigma_1 - \sigma_2}{\sigma_1 + \sigma_2} \tag{10}$$

This result shows that the stress equilibrium factor decreases to a reasonable range $|\xi| \leqslant 5\%$ at $t_{ini} = 50\ \mu s$ and this equilibrium state is broken when the time exceeds $t_{end} = 106\ \mu s$ in the post-peak stage. The perquisite of the stress equilibrium in specimen fracturing can be satisfied. The crack initiation sequence is not influenced by the stress difference at the specimen ends and therefore the suggested Brazilian tension equation can be roughly used to compute the dynamic tensile strength. The stress σ_{yy} distributions corresponding to the two critical states are plotted in Fig. 12d. At the initial equilibrium moment, the tensile stress surrounding the neutral axis is distributed uniformly as well as compression concentration beneath the contact points. After the progressive failure, the contact condition is destroyed and the stress distribution is distinct due to the local fracturing. These results make sure the reasonability of SHPB technique research on dynamic tension simulation for rocks is reasonable.

5.2 Characterization of tensile strength and failure process

The stress-time curve in association with the micro cracks evolution is shown in Fig. 13. The tensile stress increases nearly linearly with time to the peak stress of 29.5 MPa at time 78 μs. This stress is the dynamic tensile strength at this stress rate. The stress rate $\dot{\sigma}$ is taken as the slope of a linear fit to the rising portion between 10% and 90% of the peak strength and the strain rate $\dot{\varepsilon}$ is calculated by Eq.5. For this simulation, the stress rate is calculated to be 378 GPa/s and the nominal strain rate is estimated by dividing the static Young's modulus, $\dot{\varepsilon}$ =9.0 /s. The stress change with respect to time can be divided to six stages by five points (point A,

B, C, D and E) according to the fracturing characteristics of the specimen response as shown in Fig. 13. Point A is the beginning point of micro cracks generation corresponding to the crack initiation on the cumulative crack count curve. After the initiation of the pre-existed defects in the specimen, there is a dramatic eruption on the acoustic emission events at point B. This moment reveals the nucleation and interaction of the initial defects. After the peak failure, the micro fracturing frequency exceeds the maximum at point C, this moment is mobilized as the coalescence of the macro cracks and results in equilibrium destroy at the ends of the specimen. If this failure is processed, the micro rapture generation is decreased to a stable stage after point D. Point E represents the ultimate failure state after a full impact loading.

At crack initiation point in Fig. 14 ($t_a = 53\ \mu s$), the stress σ_{yy} reaches uniformity after several reverberations of the incident wave. The fractures initiated from the middle part of the specimen are dominated by intergranular tensile cracks with average orientation angle ranges of $0 \leqslant \theta < 15^{\circ}, 170^{\circ} \leqslant \theta < 180^{\circ}$. These cracks are induced by local stress concentration at the tips of the grain boundaries. When the external stress is successively applied on the specimen, these initial cracks continue to propagate and nucleate and macro cracks paralleling to the loading direction at the center of the specimen are observed. These discontinuities will result in nonuniformity of the stress distribution. From the viewpoint of the micro cracks, the intergranular tensile still dominate the micro failure, but more and more shear cracks either the intergranular shear crack or the transgranular shear crack are generated. The orientation of the tensile cracks turns to be homogeneous in the range of $0 \leqslant \theta < 30^{\circ}, 150^{\circ} \leqslant \theta < 180^{\circ}$. The dominant shear orientation is nearly 58.6° at this moment ($t_b = 69.3\ \mu s$). When the stress exceeds the failure strength ($t_c = 85.4\ \mu s$), the micro cracks furtherly coalesce and the macro fracturing cross through the specimen, some other branching cracks are generated at the same time. More transgranular tensile cracks as well as the shear cracks are induced after point C. This change continues when the loading reaches point D ($t_d = 92.3\ \mu s$). More and more cracks beneath the contact ends are generated and the specimen is fractured to two halves. Therefore the stress gap nearby the tension fracture can be observed and the compression concentrations under the contact points are released due to the indentation crush. Although all

cracks are increased during this stage but the transgranular tensile crack has a higher generation rate. The dominant shear orientations are 58.6° and 142°. When the specimen is totally ruptured at $t_e = 107\ \mu s$, the stress is released in the specimen and branching crack induced by the indentation crush successively propagates. Due to the residual kinetic of the specimen, this crush at the opposite side of the wave propagation direction seems to be more significant than that of the other side. The high speed camera snapshots obtained from the experiment at strain rate $\dot{\varepsilon} \approx 9.8\ s^{-1}$ (*Zhang and Zhao, 2013*) is illustrated here (in Fig. 15) to compare axial splitting process. This experimental fracturing time is $t_f = 75\ \mu s$ and the failure strength is $\sigma_d = 32.5\ MPa$. At time $t = 48\ \mu s$, the stress equilibrium at the ends of the specimen was achieved. The visible fracture initiates at the center of the specimen at time $t = 64\ \mu s$. This moment approximately corresponds with the point B ($t_b = 69.3\ \mu s$) in simulation. At time $t = 80\ \mu s$, this tensile fracture propagates to the contact ends and eventually coalesce at time $t = 96\ \mu s$. The comparable sequences in simulation are $t_c = 85.4\ \mu s$ and $t_d = 92.3\ \mu s$ corresponding to the generation of the macro tensile fracture. When the tensile fracture is coalesced, the crush induced by the indentation of end contacts is visible at time $t = 160\ \mu s$. This moment is comparable with the simulated stage after point E because significant shear crushes are generated at the specimen ends.

5.3 Effect of strain rate on energy transition

Bond breakage and rock fragmentation are irreversible processes associated with energy transformation and dissipation. In the modelling, the dissipated energy E_{dis} is directly computed by the friction energy E_f and the kinetic energy E_k as

$$E_f = \int \sum_{i=1}^{Nc} (\langle F_i^s \rangle \Delta u_i^{slip}) dt \tag{11}$$

$$E_k = \frac{1}{2} \sum_{i=1}^{Np} \left(m_i v_i^2 + \bar{I}_i \omega_i^2 \right) \tag{12}$$

where Nc, Np are number of the linear contact and particles in the sample. $\langle F^s \rangle$ is the average shear force and Δu_i^{slip} is the current slip increment. $m_i, v_i, \omega_i, \bar{I}_i$ are the mass, velocity components, rotation and moment of inertia of the particle. As shown in Fig. 16,

these energies e.g. the dissipated energy, the kinetic energy and the slip energy exhibit strong rate sensitivity and result in the micro fracturing transition from axial splitting to fragmentation. The kinetic energy resulted from residual movements of the particles after breakage is increased from 149 J to 445 J as the strain rate increases from 5.7 /s to 41 /s. This strain rate increase also gives a rise of the friction energy from 48 J to 205 J. The dissipated energy can be decomposed to the kinetic energy and the slip energy after failure. Most dissipated energy is consumed to the kinetic energy of the unbonded particles in dynamic loading which enhances the fragmentation of the specimen. Fig. 16d shows that the composition ratio is increased from 3% to 68% of the total dissipated energy from quasi-static loading to the dynamic loading at strain rate $\dot{\varepsilon} = 41$ /s. The friction energy reveals the crush degree under the contact points which is dominated by shear cracks.

5.4 Effect of strain rate on micro fracturing

The change of different fractures with respect to strain rates is presented in Fig. 17. The fracture number is linearly increased with the strain rate in the range of $\dot{\varepsilon} \leqslant 15$ /s. This increase is slowed down when the strain rate exceeds the critical value. In low strain rate loading, especially for the quasi-static loading, the intergranular tensile crack has absolute advantages in the failure process. The composition ratio of the intergranular tensile crack is 72% in static test and this value dramatically decreased to 51% when the strain rate is increased to 12.5 /s. The transgranular tensile crack takes the place of the intergranular tensile crack and the composition ratio is increased from 25% to 46% at the corresponding strain rate. This percent successively increases to 52% when the strain rate exceeds 41 /s. As listed in Table 3, the average transgranular tensile strength is almost four times that of the intergranular contact. Therefore, much more energy is consumed for the rupturing of the specimen at high strain rate. This result is codetermined by the evolution of the micro fracturing as well as the rupture transition from intergranular cracks to transgranular cracks. Similarly, the transition of shear fracture is also performed in dynamic tests as shown in Fig. 17a-b. From the figures, the composition ratio of shear crack is generally less than 5%. There is an increasing trend of the transgranular shear crack when the strain rate exceeds 15 /s but this change is ignorable when comparing with the tensile fractures.

The damage variable is directly defined on the cumulative area loss of the ultimate failure surface as

$$\omega = \frac{\sum_{i=1}^{n} r_i l_i}{\sum_{i=1}^{N} r_i l_i} \tag{13}$$

where N and n are the total crack number at ultimate failure and current crack number cumulated, respectively. r_i and l_i are the radius and length of the *i*th crack. Fig. 18 presents the damage evolution from the micro fracturing propagation at different strain rates. The cumulative Weibull distribution is used to characterize the damage change with respect to time as

$$\omega = 1 - \exp\left(-\frac{1}{b}\left(\frac{t}{a}\right)^{b}\right) \tag{14}$$

where a is the scale parameter determining the mean value of the distribution and b is the shape parameter determining the increase rate of the distribution. As shown in the figure, this distribution model is reasonable to describe the micro damage behaviours for rocks. The strain rate influences the parameters rather than the model itself. The scale parameter and shape parameter are illustrated in the parentheses with superscripts a and b. It can be seen that the scale parameter is decreased from 86 μs to 41μs successively when the strain rate is increased from 5.7 /s to 41/s. The corresponding value of the shape parameter in decreased from 8.5 to 5.3. This conclusion results in less width and more abrupt increase on the micro damage distribution and phenomenologically decrease the rupturing duration of the specimen. The cases of $\dot{\varepsilon}$ =10^{-5}, 12.5, 24.3 and 41 /s are performed in Fig. 19 to compare the micro crack orientation distributions. As shown in the figure, the number of the intergranular tensile crack (blue bars) is larger than that of the transgranular tensile crack (red bars) in quasi-static loading. As the strain rate increases, this difference is reduced and eventually the number of the intergranular crack exceeds that of the transgranular crack at $\dot{\varepsilon}$ =41 /s. The dominant orientation angle for tensile cracks is limited to the range of 0~30° and 150~180° parallel to the loading direction in static test which resulted in heterogeneous fracturing of the specimen. This heterogeneity is decreased under dynamic loading and the orientation is approximate to an elliptic distribution. In terms of the shear cracks, the composition ratio of the shearing

fracturing is disadvantaged throughout. Unlike the tensile cracks, both the intergranular shear cracks (black bars) and the transgranular shear cracks (green bars) are dominated in the orientation ranges of 45~60° and 130~145°. As discussed section 4.2, the shear cracks are clustered beneath the contact points and therefore the strain rate only influenced the quantity of the cracks rather than the orientation angles.

5.5 Effect of strain rate on fragment characterization

The fragment of the specimen is determined by the micro fracturing performance and to some extent influences the energy dissipation under dynamic loading. In the modelling, the fragment sequence is mobilized as all the boundary bonds of the assembly are ruptured and the clustered particles turn to be an independent island. Fig. 20 presents the fragment states at different strain rates. The color of the particles represents the sequence of the fragment and the increased color number indicates the fragmentation degree of the specimen. The static loading commonly results in perfect and smooth splitting along the neutral axis. As the strain rate increases, these changes mainly focus on the branching of the dominant tensile surface and the indentation crush beneath the contact ends. The branching crack induced by the failure of the intergranular tensile cracks propagates and eventually coalesces with the tensile surface which results in fragments in the middle of the disc. The crush under the contact points is caused by the compression concentration and strengthens the transgranular failure within the mineral grains. This indentation also results in further fragmentation of loading ends. The fragment size distribution is plotted in Fig. 21a and the 50% probability fragment size change with respect to strain rate is shown in Fig. 21b. In Brazilian test, the main fragments separating the disc two halves commonly have dominant size which takes 90% part of the specimen volume. The other fragments are pulverized to smaller size under dynamic loading. From the decrease of the 50% probability fragment size with respect to strain rate in Fig. 21b, this average size changes from 104.4 mm^3 at static loading to 11.2 mm^3 when the strain rate exceeds 41 /s. The experiment results (red dots) were carried out by sieving test to compare the fragmentation in dynamic Brazilian test. This dynamic fragmentation can be characterized by the power function $d_{50} = 1/(a + b\dot{\varepsilon}^c)$ and the parameters are illustrated in

the figure.

Fig. 22 shows the micro cracks distribution and the schematic of the failure pattern at the cases of $\dot{\varepsilon}=10^{-5}$, 12.5, 24.3 and 41 /s. At static loading, the figure shows a major tensile splitting along the loaded axis of the specimen and substantial damage surrounding the splitting surface. This tensile fracture is mainly composed by the intergranular tensile cracks. At strain rate $\dot{\varepsilon}=12.5$ /s, apart from the dominant splitting fracture, indentation induced shear crushes are observed under the contact points. The splitting surface is codetermined by the intergranular tensile crack and the transgranular crack. When the strain rate is increased to $\dot{\varepsilon}=24.3$ /s, the indentation crush zones are expanded and the branching crack induced by the propagation of the intergranular tensile cracks coalesces with the splitting surface. This coalescence results in local fragment nearby the splitting surface and eventually increases the fragmentation of the specimen. The splitting zone is no longer smooth and the branching cracks cause further complicated failure surrounding the loaded axis. The crushed zone propagates to the main tensile fracture and crushing bands can be observed throughout the specimen.

To compare with simulated results, polarized microphotographs of sample $\dot{\varepsilon}=14$/s were carried out. The full scale image of the main crack is captured in Fig. 23a on plane polarized mode and that of crossed polarized image is presented in Fig. 23b. The macro cracks are mainly existed as the splitting crack with less branching cracks and the indentation crush core. Because the indentation cores were crushed to pulverization, these areas are filled with epoxy resins and no mineral components and microstructures can be observed. The enlarged image of the splitting crack is presented in Fig. 23c and the transgranular cracks through quartz and feldspar are highlighted by red arrows. From this figure, the main crack in splitting test is codetermined by the transgranular and intergranular cracks. In most cases, the main crack propagates as a straight line and does not branch or buckling when meets heterogeneous mineral components. Widely distributed microcracks can be observed within grains which surround the main crack as shown in Fig 23d-e, the clustered tensile cracks fracture through the whole mineral grain and in turn cause grain pulverization. Additionally, the shear induced crack bands can be found in Fig 23f-g. The shear cracks are commonly existed as

transgranular cracks with large amount of branching cracks. The enlarge images of transgranular and intergranular cracks are also presented in Fig. 23h-g with highlighted labelled arrows.

On as smaller scale, the scanning electron microscope images on sample $\dot{\varepsilon}$=14/s are shown in Fig. 24. The cracks existed in debris can be observed on the 1,000X-magnification images. Tensile cracks are generated smoothly and nearby grains keep unbroken from the 10 μm scale images in Fig. 24a-b. Contrary results can be found for shear crack as shown in Fig. 24c-d. Grain pulverization under dynamic loading is a common phenomenon and this result is believed to be induced by dynamic shearing. Shear-induced tensile cracks are widely distributed in grains and derive the fragmentation for grains (*Aben et al., 2016*).

5.6 The scaling of rate dependent tensile strength

Strain-rate dependency is a macro-response for rocks when subjected to dynamic loading. *Schindler (1968)* performed that particle rearrangements including the contact sliding and particle rotation are major contributors to the strain rate effect for granular materials. *Huang et al (2014b)* presented that the grains have no enough time to accumulate elastic energy and drive cracks to propagate along the pre-existed defects. Therefore, the breakage of each grain produces more fragments and more degrees of freedom in the granular debris that result in larger energy dissipation subjected to dynamic loading. Fig. 25 presents the tensile stress change with respect to strain or time at different impact velocities. As expected, the stress-strain behaviours exhibit a general increase at increased strain rates for granular rocks. It should be noted that the strain listed herein is the axial strain of the disc rather than the tensile strain perpendicular to the loading axis. From the change of the stress with respect to time in Fig. 25b, the increased impact velocities induces larger stress rate and at the same time improves the failure strength of the rocks. In this study, the rate dependency is characterized as the ratio of dynamic Brazilian strength to static Brazilian strength ($DIF = \sigma_{td}/\sigma_t$). A summary of the available experimental data for different rocks in dynamic tension tests is presented in Fig. 26a-b. In the figure, the direct tension results (shown as solid dots) show lower rate sensitivity in comparing with the results carried out by other indirect methods. The spalling tests (half-solid dots) have the largest values of the dynamic increase

factor due to the coupling of the inertia stress in the fractured strength. Kimberley et al (2013) proposed a rate dependent strength model incorporating fundamental physics including the crack initiation, propagation and nucleation for brittle materials. In his model, the dynamic increase factor is defined by the power law of the characteristic strain rate $\dot{\varepsilon}_0$ as

$$DIF = 1 + \left(\frac{\dot{\varepsilon}}{\dot{\varepsilon}_0}\right)^{2/3} \tag{15}$$

Li et al (2018) discussed the reasonability of this model and gave a more appropriate form for the tension test as

$$DIF = 1 + \left(\frac{\dot{\varepsilon}}{\dot{\varepsilon}_0}\right)^{\alpha} \tag{16}$$

where α is the increase rate parameter in the range of (0,1] for rocks. This value is generally determined by the fracturing types e.g. tension test and compression test and the intrinsic properties e.g. crack density, heterogeneity and integrity of the samples. In Kimberley's model, the characteristic strain rate $\dot{\varepsilon}_0$ can be estimated by:

$$\dot{\varepsilon}_0 = \lambda \frac{v_c K_{IC} \eta^{1/4}}{\bar{s} E} \tag{17}$$

where λ is a dimensionless proportionality constant which is usually taken as λ=2.4 and K_{IC} is the mode I fracture toughness. v_c is the limiting crack growth speed which is equal to the Rayleigh wave velocity. η and $\bar{s}$ are initial defects parameters and are computed from the distribution of the defects. The term E is the Young's modulus of the material. This characteristic strain rate $\dot{\varepsilon}_0$ gives a critical point that the dynamic increase factor is 2.0 when the strain rate equals to the characteristic value. From the regression results of different rocks shown in Fig. 26b, the $\dot{\varepsilon}_0$ varies from 0.15 to 2.1 /s for different rock types. The increase rate factor α ranges from 0.35 to 0.63. It is found that the nominalized dynamic tensile strengths of tuff and basalt are higher than that of other rock types. On the other hand, these two rocks have lowest characteristic strain rate values of 0.15 and 0.21 /s, respectively. The chondrite is most sensitive to high strain rate with highest α value of 0.63. The estimated results of granites are $\dot{\varepsilon}_0$=2.1 /s and α=0.53. Considering the experimental results are carried out in different conditions with different specimen size, these results cannot be fully used to characterize the researched rocks. The simulated results as well as the experiments are presented in Fig. 26c. It is found that the granite shows little variation in tensile strength at

low strain rate ($\dot{\varepsilon}\sim 1.0$ /s), but shows significant enhancement in strength when the strain rate exceeds the characteristic strain rate $\dot{\varepsilon}_0$ =5.0 /s. The simulated results show reasonable agreement with the experiments and the increase rate parameter α is about 0.78.

6. Conclusion

Dynamic Brazilian disc tests are carried out on the granites at different strain rates with the SHPB apparatus. Three strain gauges are mounted on the specimen surface to investigate the fracture sequence of the specimen. The experimental results show that the tensile strength of rocks is sensitive to strain rate. At lower strain rate, the stress equilibrium state is satisfied preceding the crack initiation and results in sequential fracturing of the splitting crack in the specimen. This prerequisite is broken after the indentation crush beneath the loaded end as the loading rate is further increased. The inertia stress promotes the unbalanced movement of the specimen and eventually acts on the transmitted wave as a platform.

In order to characterize the dynamic strength and fragment behaviours for rocks from the viewpoints of micro fracturing, a realistic modelling of the micro heterogeneity for rocks is performed on the basis of grain-based discrete element method. The microstructure of the specimen is reproduced by the digital image processing of mineral scanning for rocks directly at grain scale. The mechanical behaviours on the grain boundaries and intra grains are performed as intergranular and transgranular contacts with different contact constitutive relations. This model is shown to be reasonable in simulation of dynamic tension test on granite. The simulated results either on the tensile strengths or on failure fragments are comparable with experiments. The stress equilibrium validity is systemically discussed from the three-wave superposition, crack propagation sequences, end forces as well as the stress distribution in the specimen. The simulated results show that the micro fracturing can be divided into six stages as crack initiation, propagation, coalesce, branching and indentation crush in the dynamic loading. The micro fracturing characteristics dependent on the strain rate give rise of dissipated energy and in turn strengthen the sustainability of the specimen. The increased external energy promotes the further fracturing of the specimen with a transition from the intergranular cracks to transgranular cracks. A Weibull model for presenting the

micro damage evolution is derived and the strain rate decreases both the scale and shape parameters which results in more abrupt growth of the fracturing. Besides, the dynamic loading induces a crack orientation transition from the range of 0~30°, 150~180° to a homogenous distribution in tension failure.

These micro fracturing transitions are the intrinsic mechanism of the strain rate effect for rock materials and in turn resulting in fragmentation transition from sparse fracture to pervasive pulverization. The 50% probability fragment size change with the strain rate indicates the higher velocity impact improves the breakage of the specimen. These failure patterns can be categorized into four types when the loading condition varied from the static to the high strain rate loading. Apart from the shear crush induced by the bars indentation, the branching cracks nearby the splitting surface as well as the pulverization of grains beneath the loaded points are observed as the strain rate increases. The simulated tensile strengths are consistent well with experiments and further confirm the reasonability of the model. The dynamic increase factor shows a general scaling law presented by the characteristic strain rate and the increase rate. In this study, the characteristic strain rate is 5.0 and the increase rate factor is 0.78 for the granite.

Acknowledgement

This work was supported by National Natural Science Foundation of China (Nos. 51439008, 51679231 and 41572307) and China Scholarship Council (to the first author, No. 201604910678).

Reference:

Aben F M, Doan M L, Mitchell T M, et al. Dynamic fracturing by successive coseismic loadings leads to pulverization in active fault zones[J]. Journal of Geophysical Research: Solid Earth, 2016, 121(4): 2338-2360.

Asprone D, Cadoni E, Prota A, et al. Dynamic behavior of a Mediterranean natural stone under tensile loading[J]. International Journal of Rock Mechanics and Mining Sciences, 2009, 46(3): 514-520.

Bahrani N, Kaiser P K, Valley B. Distinct element method simulation of an analogue for a highly interlocked, non-persistently jointed rockmass[J]. International Journal of Rock Mechanics and Mining Sciences, 2014, 71: 117-130.

Bahrani N, Kaiser P K. Estimation of Confined Peak Strength of Crack-Damaged Rocks[J]. Rock Mechanics and Rock Engineering, 2017, 50(2): 309-326

Bhat H S, Rosakis A J, Sammis C G. A micromechanics based constitutive model for brittle failure at high strain rates[J]. Journal of Applied Mechanics, 2012, 79(3): 031016.

Cadoni E. Dynamic characterization of orthogneiss rock subjected to intermediate and high strain rates in tension[J]. Rock Mechanics and Rock Engineering, 2010, 43(6): 667-676.

Cai M, Kaiser P K, Suorineni F, et al. A study on the dynamic behavior of the Meuse/Haute-Marne argillite[J]. Physics and Chemistry of the Earth, Parts A/B/C, 2007, 32(8): 907-916.

Chen R, Dai F, Qin J, et al. Flattened Brazilian disc method for determining the dynamic tensile stress-strain curve of low strength brittle solids[J]. Experimental Mechanics, 2013, 53(7): 1153-1159.

Cho S H, Ogata Y, Kaneko K. Strain-rate dependency of the dynamic tensile strength of rock[J]. International Journal of Rock Mechanics and Mining Sciences, 2003, 40(5): 763-777.

Cundall P A, Strack O D L. A discrete numerical model for granular assemblies[J]. geotechnique, 1979, 29(1): 47-65.

Dai F, Huang S, Xia K, et al. Some fundamental issues in dynamic compression and tension tests of rocks using split Hopkinson pressure bar[J]. Rock mechanics and rock engineering, 2010(a), 43(6): 657-666.

Dai F, Xia K, Luo S N. Semicircular bend testing with split Hopkinson pressure bar for measuring dynamic tensile strength of brittle solids[J]. Review of Scientific Instruments, 2008, 79(12): 123903.

Dai F, Xia K, Tang L. Rate dependence of the flexural tensile strength of Laurentian granite[J]. International Journal of Rock Mechanics and Mining Sciences, 2010, 47(3): 469-475.

Dai F, Xia K. Loading rate dependence of tensile strength anisotropy of Barre granite[J]. Pure and applied geophysics, 2010(b), 167(11): 1419-1432.

Dutta P K, Kim K. High-strain-rate tensile behavior of sedimentary and igneous rocks at low temperatures[R]. Cold regions research and engineering lab hanover nh, 1993.

Fang X, Xu J. A Modified Overstress Model to Simulate Dynamic Split Tensile Tests and Its Experimental Validation[J]. Rock Mechanics and Rock Engineering, 2016, 49(9): 3823-3828.

Farahmand K, Diederichs M S. Hydro-Mechanical Effects of Pore Pressure on Deformability and Fracture Strength of Rock: A Numerical Modeling Study[C]//50th US Rock Mechanics/Geomechanics Symposium. American Rock Mechanics Association, 2016.

Farahmand K, Vazaios I, Diederichs M S, et al. Investigating the scale-dependency of the geometrical and mechanical properties of a moderately jointed rock using a synthetic rock mass (SRM) approach[J]. Computers and Geotechnics, 2018, 95: 162-179.

Goldsmith W, Sackman J L, Ewerts C. Static and dynamic fracture strength of Barre granite[C]//International Journal of Rock Mechanics and Mining Sciences & Geomechanics Abstracts. Pergamon, 1976, 13(11): 303-309.

Gomez J T, Shukla A, Sharma A. Static and dynamic behavior of concrete and granite in tension with damage[J]. Theoretical and Applied Fracture Mechanics, 2001, 36(1): 37-49.

Gong F Q, Zhao G F. Dynamic indirect tensile strength of sandstone under different loading rates[J]. Rock mechanics and

rock engineering, 2014, 47(6): 2271-2278.

Grady D E, Kipp M E. Continuum modelling of explosive fracture in oil shale[C]//International Journal of Rock Mechanics and Mining Sciences & Geomechanics Abstracts. Pergamon, 1980, 17(3): 147-157.

Grady D E. Local inertial effects in dynamic fragmentation[J]. Journal of Applied Physics, 1982, 53(1): 322-325.

Gui Y L, Bui H H, Kodikara J, et al. Modelling the dynamic failure of brittle rocks using a hybrid continuum-discrete element method with a mixed-mode cohesive fracture model[J]. International Journal of Impact Engineering, 2016, 87: 146-155.

Hogan J D, Kimberley J, Hazeli K, et al. Dynamic behavior of an ordinary chondrite: The effects of microstructure on strength, failure and fragmentation[J]. Icarus, 2015, 260: 308-319.

Hong L, Zhou Z, Yin T, et al. Energy consumption in rock fragmentation at intermediate strain rate[J]. Journal of Central South University of Technology, 2009, 16(4): 677-682.

Howe S P, Goldsmith W, Sackman J L. Macroscopic static and dynamic mechanical properties of Yule marble[J]. Experimental Mechanics, 1974, 14(9): 337-346.

Huang J, Xu S, Hu S. Influence of particle breakage on the dynamic compression responses of brittle granular materials[J]. Mechanics of Materials, 2014b, 68: 15-28.

Huang S, Liu H, Xia K. A dynamic ball compression test for understanding rock crushing[J]. Review of Scientific Instruments, 2014a, 85(12): 123902.

Huang S, Xia K, Yan F, et al. An experimental study of the rate dependence of tensile strength softening of Longyou sandstone[J]. Rock mechanics and rock engineering, 2010, 43(6): 677-683.

Johnson J C. The hustrulid bar-a dynamic strength test and its application to the cautious blasting of rock[M]. The University of Utah, 2010.

Khan A S, Irani F K. An experimental study of stress wave transmission at a metallic-rock interface and dynamic tensile failure of sandstone, limestone, and granite[J]. Mechanics of Materials, 1987, 6(4): 285-292

Kimberley J, Ramesh K T, Daphalapurkar N P. A scaling law for the dynamic strength of brittle solids[J]. Acta Materialia, 2013, 61(9): 3509-3521.

Kubota S, Ogata Y, Wada Y, et al. Estimation of dynamic tensile strength of sandstone[J]. International Journal of Rock Mechanics and Mining Sciences, 2008, 45(3): 397-406

Kumar A. The effect of stress rate and temperature on the strength of basalt and granite[J]. Geophysics, 1968, 33(3): 501-510.

Lan H, Martin C D, Hu B. Effect of heterogeneity of brittle rock on micromechanical extensile behavior during compression loading[J]. Journal of Geophysical Research: Solid Earth, 2010, 115(B1).

Li L, Lee P K K, Tsui Y, et al. Failure process of granite[J]. International Journal of Geomechanics, 2003, 3(1): 84-98.

Li X F, Li H B, J Zhao. Reasonability of Grain-based discrete element method (GBDEM) on SHPB simulation and its application for granular rocks. Rock mechanics and rock engineering, 2017 (submitted)

Li X F, Li H B, Liu Y Q, et al. Numerical simulation of rock fragmentation mechanisms subject to wedge penetration for TBMs[J]. Tunnelling and Underground Space Technology, 2016, 53: 96-108.

Mahabadi O K, Cottrell B E, Grasselli G. An example of realistic modelling of rock dynamics problems: FEM/DEM simulation of dynamic Brazilian test on Barre granite[J]. Rock mechanics and rock engineering, 2010, 43(6): 707-716.

Rabczuk T, Belytschko T. Cracking particles: a simplified meshfree method for arbitrary evolving cracks[J]. International Journal for Numerical Methods in Engineering, 2004, 61(13): 2316-2343.

Rabczuk T, Ren H. A peridynamics formulation for quasi-static fracture and contact in rock[J]. Engineering Geology, 2017, 225: 42-48.

Rougier E, Knight E E, Broome S T, et al. Validation of a three-dimensional finite-discrete element method using experimental results of the split Hopkinson pressure bar test[J]. International Journal of Rock Mechanics and Mining

Sciences, 2014, 70: 101-108.

Saksala T, Brancherie D, Harari I, et al. Combined continuum damage-embedded discontinuity model for explicit dynamic fracture analyses of quasi-brittle materials[J]. International Journal for Numerical Methods in Engineering, 2015, 101(3): 230-250.

Saksala T, Hokka M, Kuokkala V T, et al. Numerical modeling and experimentation of dynamic Brazilian disc test on Kuru granite[J]. International Journal of Rock Mechanics and Mining Sciences, 2013, 59: 128-138.

Schindler L. Design and evaluation of a device for determining the one-dimensional compression characteristics of soils subjected to impulse-type loads[r]. Army engineer waterways experiment station Vicksburg miss, 1968.

Schultz P H, Eberhardy C A, Ernst C M, et al. The Deep Impact oblique impact cratering experiment[J]. Icarus, 2007, 191(2): 84-122.

Tan X, Konietzky H, Chen W. Numerical Simulation of heterogeneous rock using discrete element model based on digital image processing[J]. Rock Mechanics and Rock Engineering, 2016, 49(12): 4957-4964.

Wang Q Z, Li W, Song X L. A method for testing dynamic tensile strength and elastic modulus of rock materials using SHPB[J]. Pure and Applied Geophysics, 2006, 163(5-6): 1091-1100.

Wang Q Z, Li W, Xie H P. Dynamic split tensile test of flattened Brazilian disc of rock with SHPB setup[J]. Mechanics of Materials, 2009, 41(3): 252-260.

Wong L N Y, Zou C, Cheng Y. Fracturing and failure behavior of Carrara marble in quasistatic and dynamic Brazilian disc tests[J]. Rock mechanics and rock engineering, 2014, 47(4): 1117-1133.

Wu B, Yao W, Xia K. An Experimental Study of Dynamic Tensile Failure of Rocks Subjected to Hydrostatic Confinement[J]. Rock Mechanics and Rock Engineering, 2016, 49(10): 3855-3864.

Xu Y, Dai F, Xu N W, et al. Numerical investigation of dynamic rock fracture toughness determination using a semi-circular bend specimen in split Hopkinson pressure bar testing[J]. Rock Mechanics and Rock Engineering, 2016, 49(3): 731-745.

Yan F, Feng X T, Chen R, et al. Dynamic tensile failure of the rock interface between tuff and basalt[J]. Rock mechanics and rock engineering, 2012, 45(3): 341-348.

Yu Y, Zhang J, Zhang J. A modified Brazilian disk tension test[J]. International Journal of Rock Mechanics and Mining Sciences, 2009, 46(2): 421-425.

Yuan F, Prakash V, Tullis T. Origin of pulverized rocks during earthquake fault rupture[J]. Journal of Geophysical Research: Solid Earth, 2011, 116(B6).

Yue Z Q, Chen S, Tham L G. Finite element modeling of geomaterials using digital image processing[J]. Computers and Geotechnics, 2003, 30(5): 375-397.

Zhang Q B, Zhao J. A review of dynamic experimental techniques and mechanical behaviour of rock materials[J]. Rock mechanics and rock engineering, 2014, 47(4): 1411-1478

Zhang Q B, Zhao J. Determination of mechanical properties and full-field strain measurements of rock material under dynamic loads[J]. International Journal of Rock Mechanics and Mining Sciences, 2013, 60: 423-439.

Zhao G F, Russell A R, Zhao X, et al. Strain rate dependency of uniaxial tensile strength in Gosford sandstone by the Distinct Lattice Spring Model with X-ray micro CT[J]. International Journal of Solids and Structures, 2014, 51(7-8): 1587-1600.

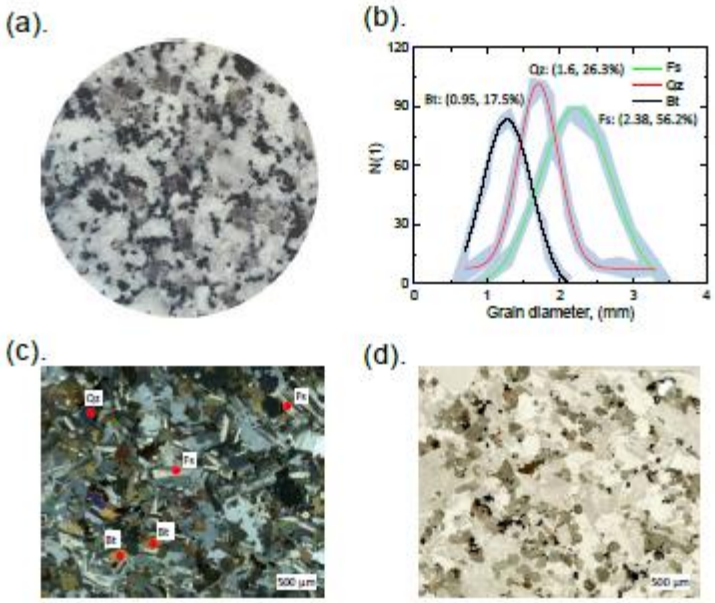

Figure. 1. (a) Surface of the granite sample showing the mineral grains. (b) The grain number distributions with varying grain size for the granite sample. (c,d) Microphotographs of the granite sample taken with crossed polarizer (Figure 1c) and plane polarizer (Figure 1d). Bt=biotite, Fs=feldspar, Qz=Quartz.

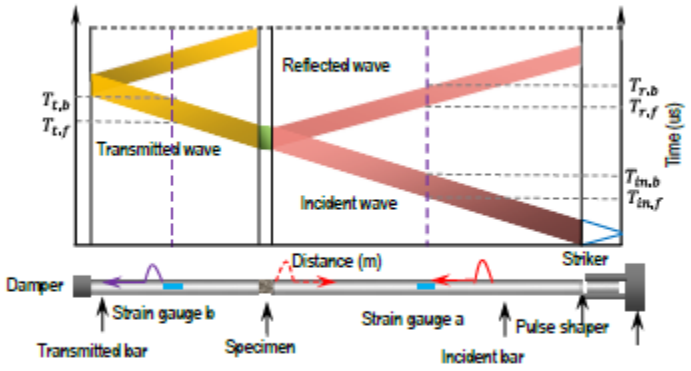

Figure. 2. Schematic of the Split Hopkinson Pressure Bar system and the wave propagation in bars.

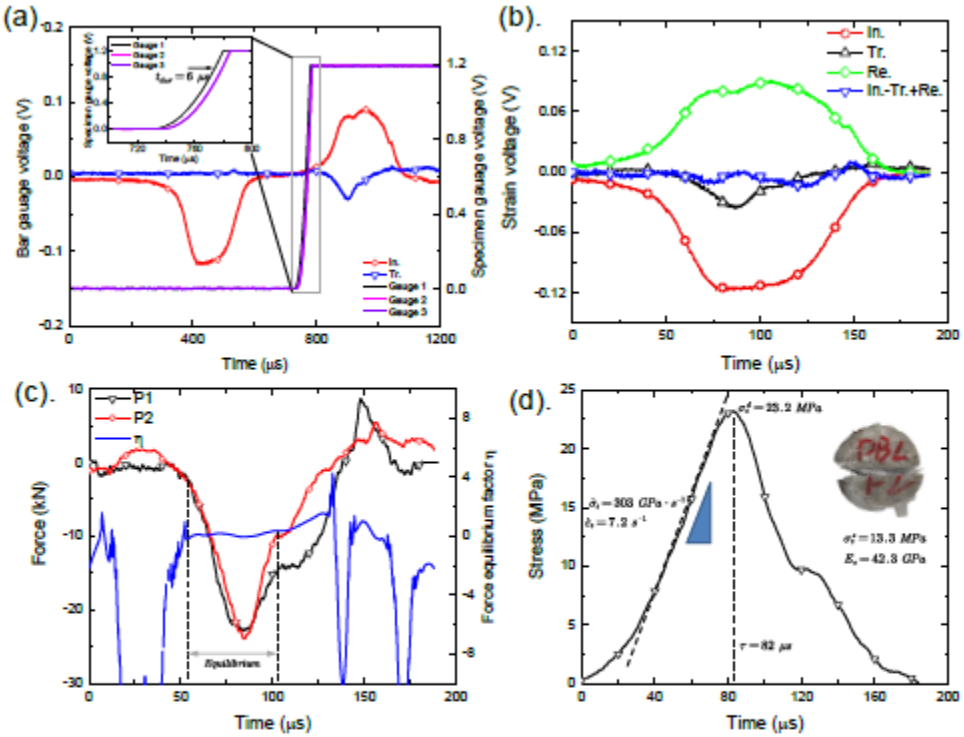

Figure. 3. Experiential results of the dynamic Brazilian disc test at $\dot{\varepsilon}$ =7.2 /s. (a) Raw data recorded from the gauges mounted on the bars and the specimen. (b) The incident (In.), reflected (Re.), transmitted (Tr.) and superposed (In.+Re.-Tr.) waves after the time shift by three-wave method. (c) Recorded forces at the ends of the specimen and the force equilibrium state in the specimen. (d) Time history of the tensile stress and the ultimate specimen failure state.

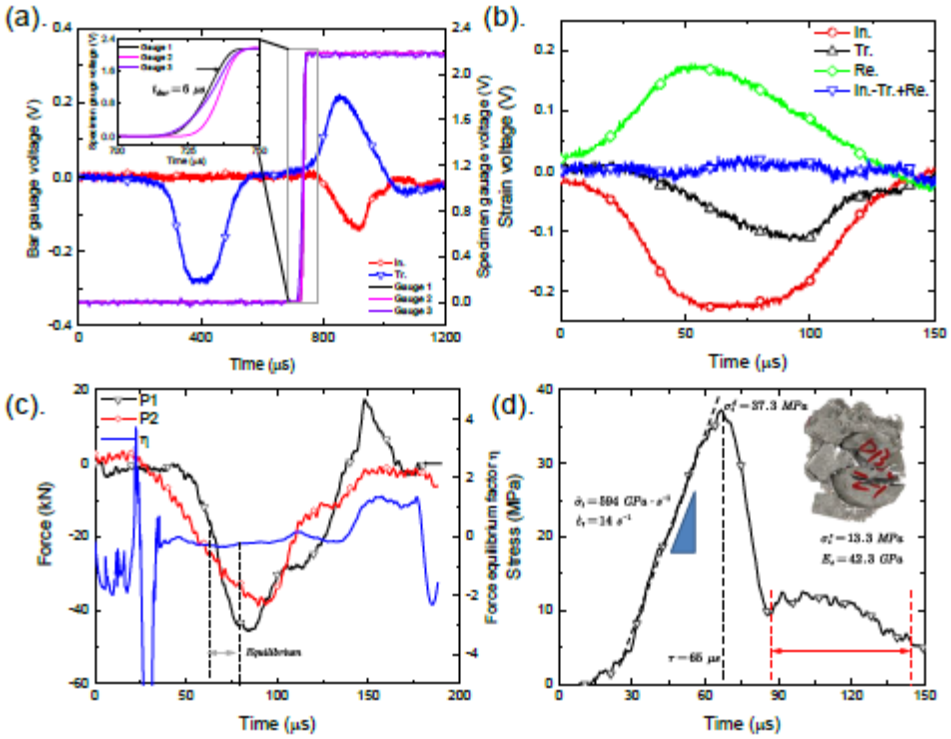

Figure. 4. Experiential results of the dynamic Brazilian disc test at $\dot{\varepsilon} = 14$ /s. (a) Raw data recorded from the gauges mounted on the bars and the specimen. (b) The incident (In.), reflected (Re.), transmitted (Tr.) and superposed (In.+Re.-Tr.) waves after the time shift by three-wave method. (c) Recorded forces at the ends of the specimen and the force equilibrium state in the specimen. (d) Time history of the tensile stress and the ultimate specimen failure state.

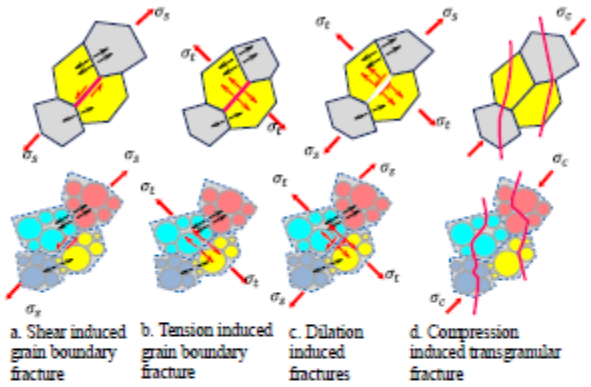

Figure. 5. Typical failure patterns among mineral grains for rocks. (a) Shearing fracture on the grain boundaries. (b) Tensile fracture on the grain boundaries. (c) Dilation induced fractures among grains. (d) Transgranular fractures within grains (Modified after *Li et al., 2016*).

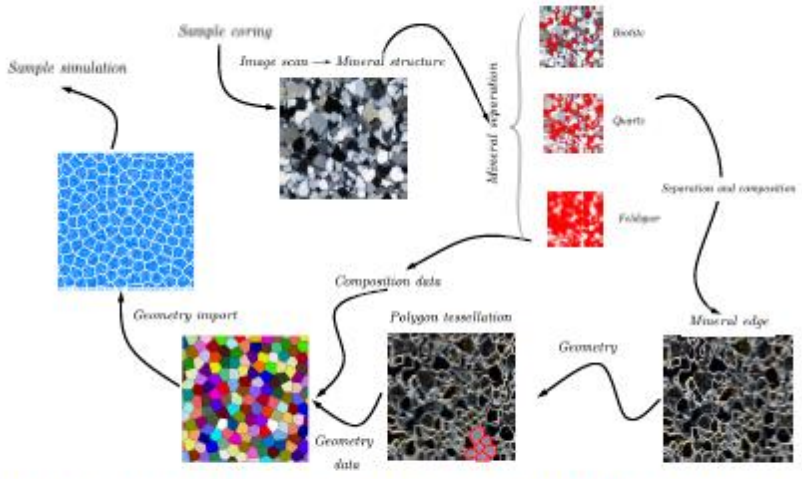

Figure 6. Flow chart of the generation of the grain-based model. Methology is used to generate polygons on the basis of realistic grain distribution in combination of image scanning technique.

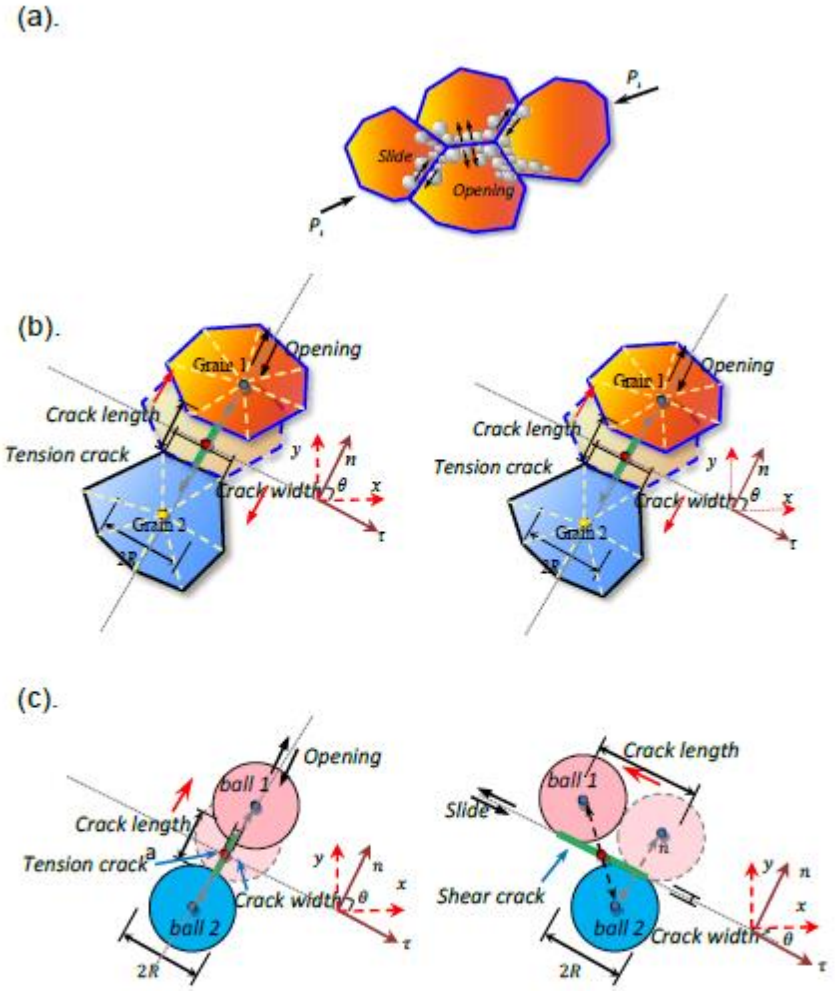

Figure 7. Schematic of the two scale grain-based discrete element model. (a). The basic granular model for four adjacent grains. (b). The grain scale polygon models and failure types among grains. (c) The particle based models within grains and failure types between particles.

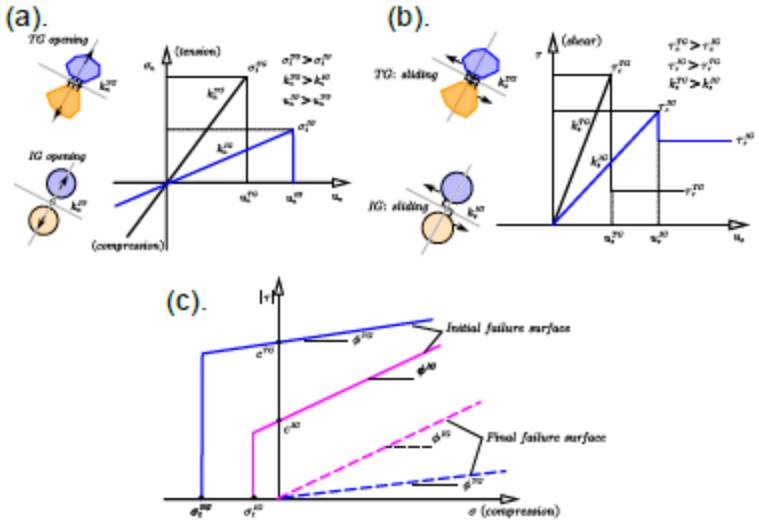

Figure. 9. The constitutive model of the contact in GB-DEM. (a) Tensile behaviour of the intergranular and transgranular contacts. (b) Shear behaviour of the intergranular and transgranular contacts. (c). The strength envelopes of the intergranular and transgranular contacts.

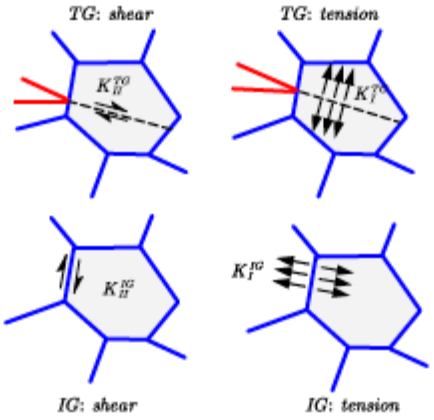

Figure. 9. Four typical failure modes in GBDEM including the trangranular shear crack (TG: shear), transgranular tensile crack (TG: tension), intergranular shear crack (IG: shear) and intergranular tensile crack (IG: tension).

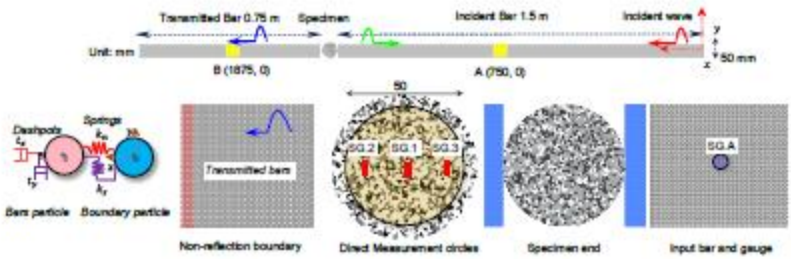

Figure. 10. The numerical model of the SHPB test for Brazilian disc rocks.

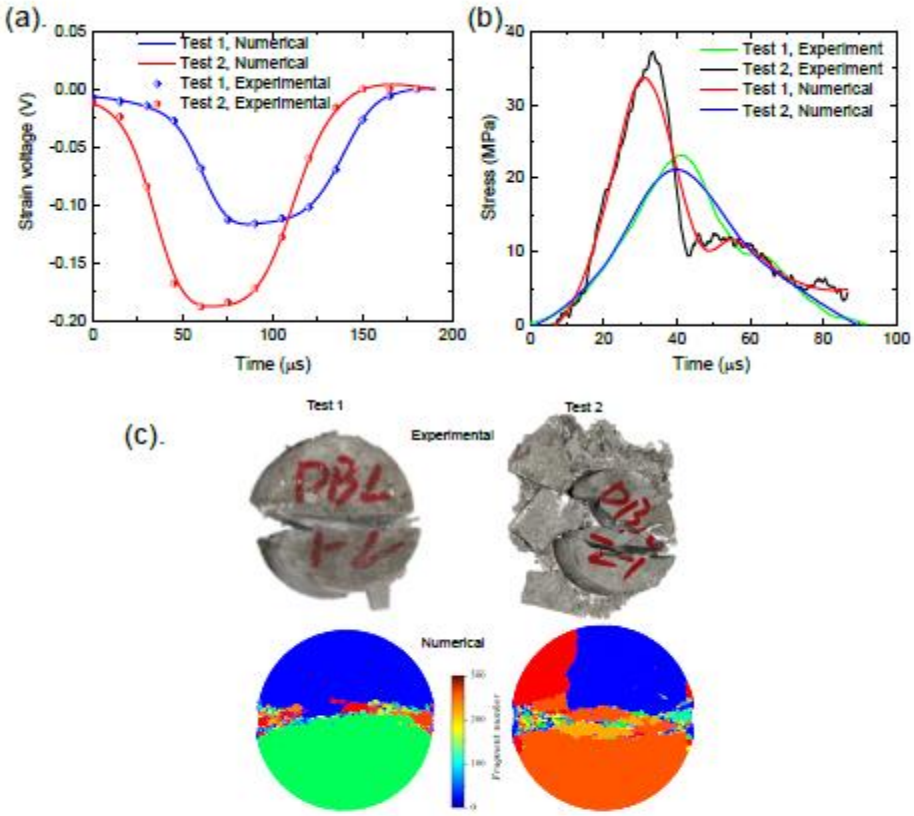

Figure. 11. (a) Experimental incident stress waves and their fitting curves applied at the end of the incident bar. (b). The comparison of the tensile stress with respect to time between the experimental and the simulated results. (c). The ultimate failure states of the granite samples at two strain rates from experiment and simulation.

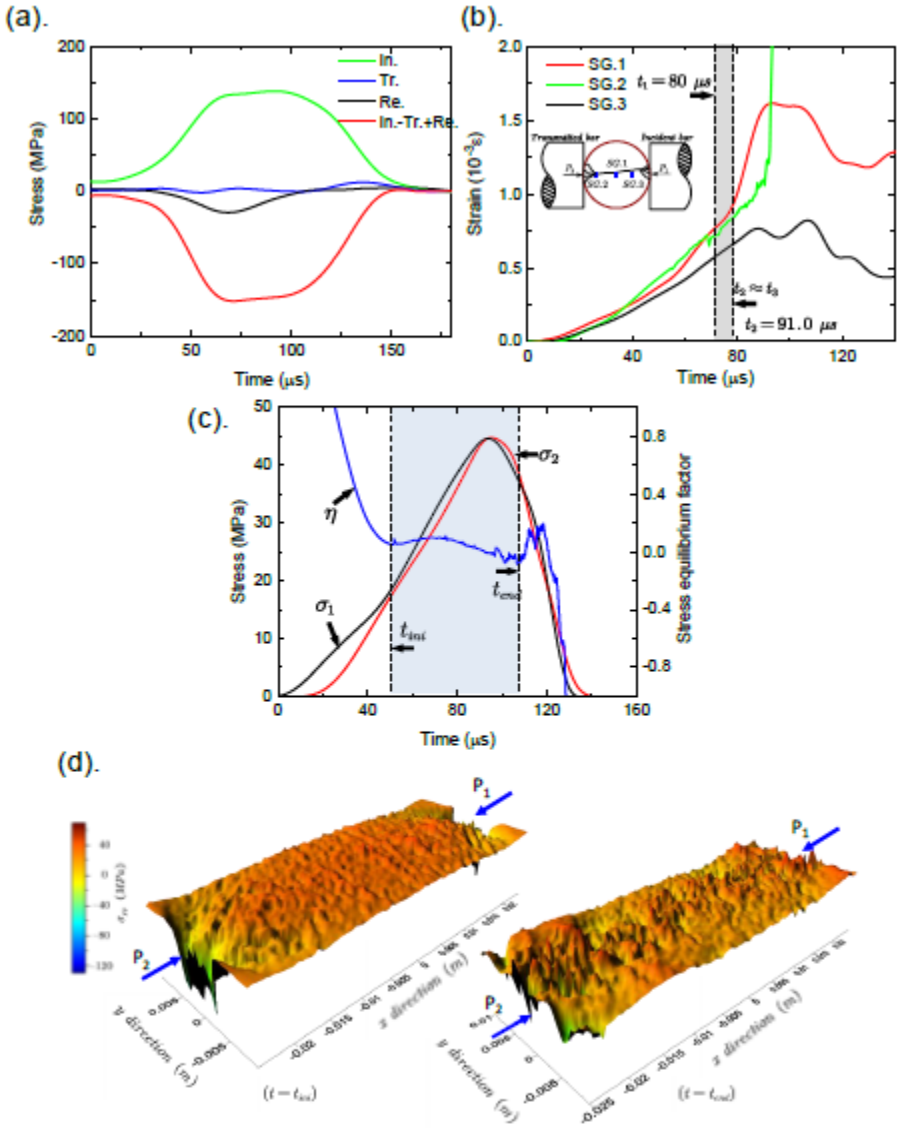

Figure. 12. The validity of the stress equilibrium state at the simulated specimen ends. (a). The incident (In.), reflected (Re.), transmitted (Tr.) and superposed (In.+Re.-Tr.) waves after the time shift by three-wave method. (b) The strain change of the specimen obtained by the strain gauges on the specimen. (c) The direct forces at the ends of the specimen and the equilibrium stress factor. (d) The stress σ_n distribution nearby the neutral loading axis of the specimen at two moments.

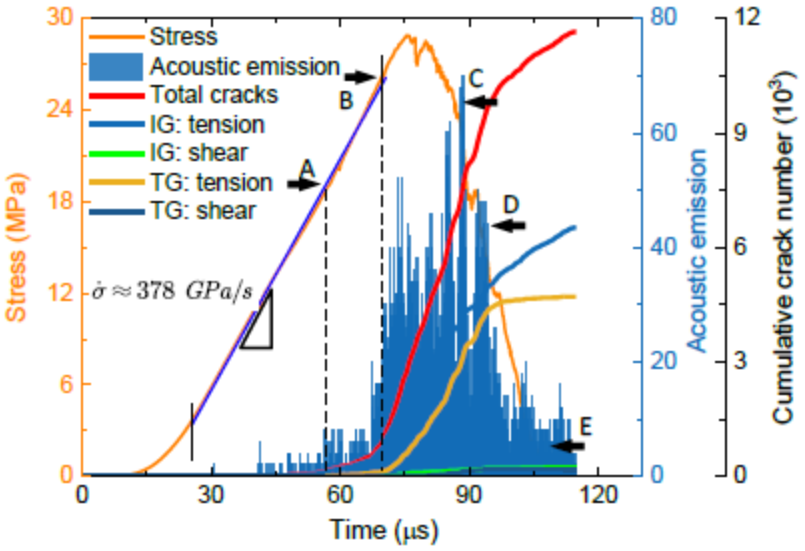

Figure 13. The simulated stress and micro crack histories of the specimen subject to dynamic tension loading

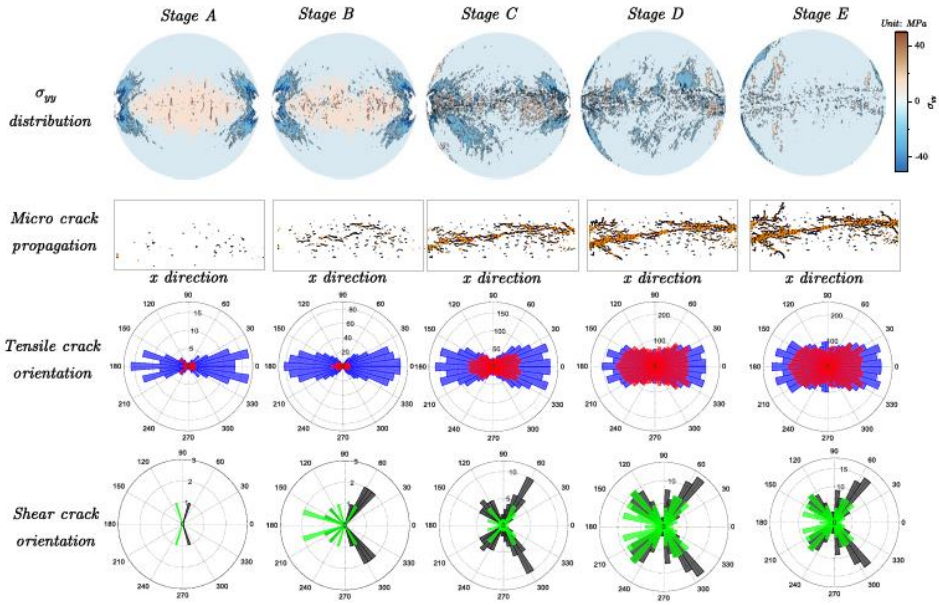

Figure. 14. The transitions of the stress field σ_{yy}, micro crack distribution and crack orientation at five moments corresponding to Stage A, B, C, D and E in Fig. 15. In the crack distribution, black IG: tension, blue IG: shear, orange TG: tension, green TG: shear. In the crack orientation, red is the TG: tension crack, blue is the IG: tension crack, black is the TG: shear crack and green is the IG: shear crack.

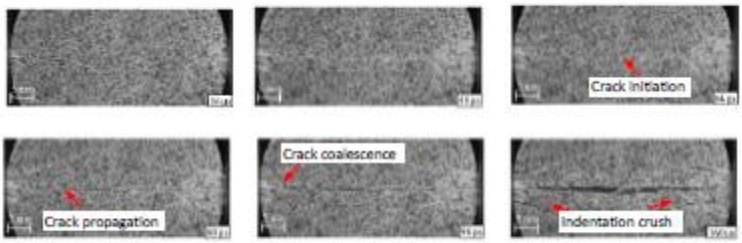

Figure. 15. Captured failure sequences by high speed camera for rock in dynamic Brazilian disc test. (modified from Zhang and Zhao, 2013).

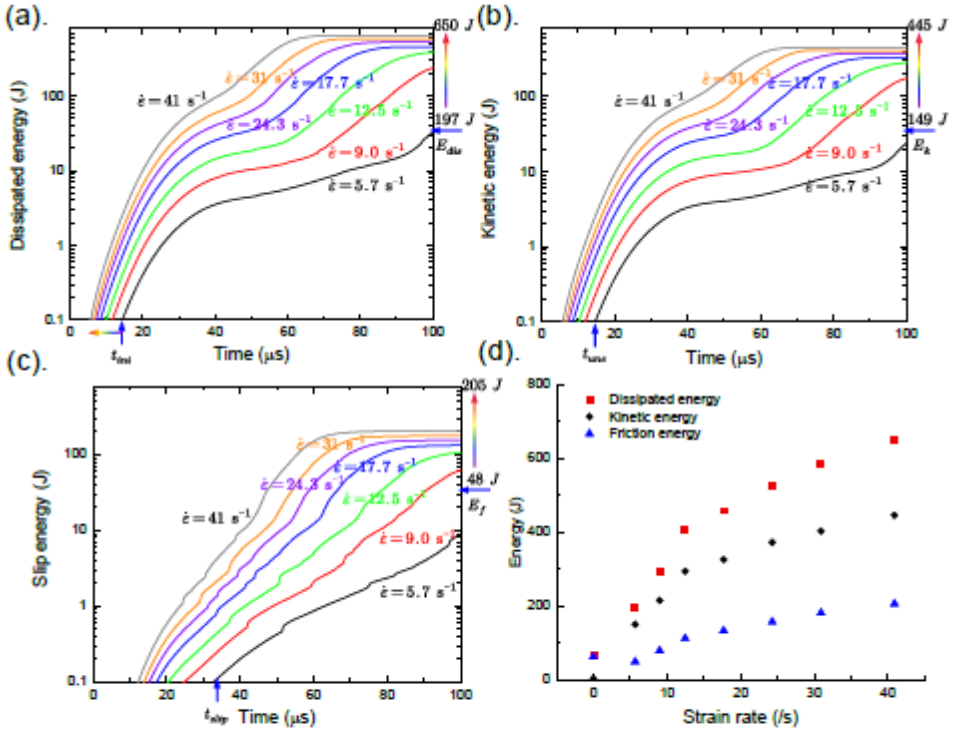

Figure. 16. Energy transition in dynamic test at different strain rates. (a). The dissipated energy. (b) The kinetic energy. (c) The slip energy. (d) The energy transition at different strain rates.

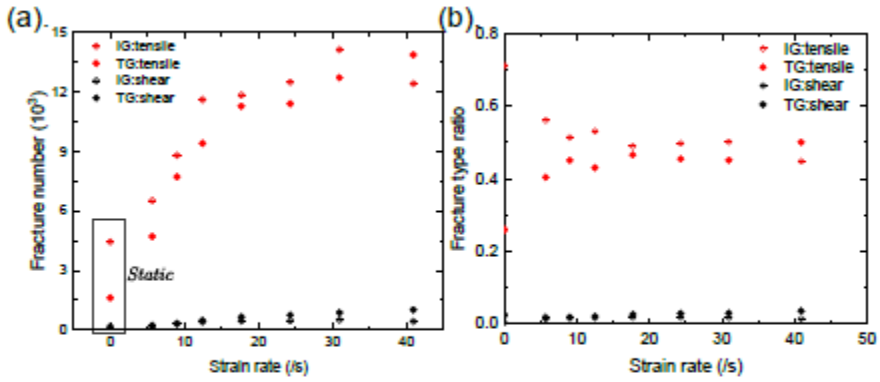

Figure. 17. Fracture number change and fracture type ratio at different strain rates.

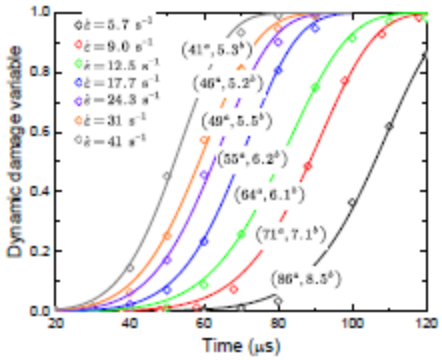

Figure. 18. The dynamic damage as a function of time at different strain rates.

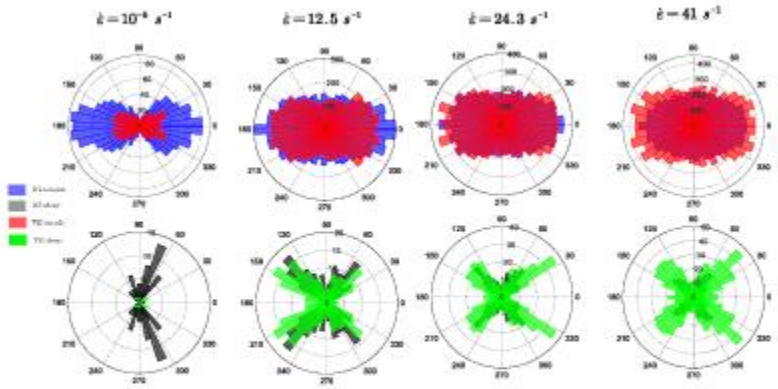

Figure. 19. The crack orientation distribution at four strain rates.

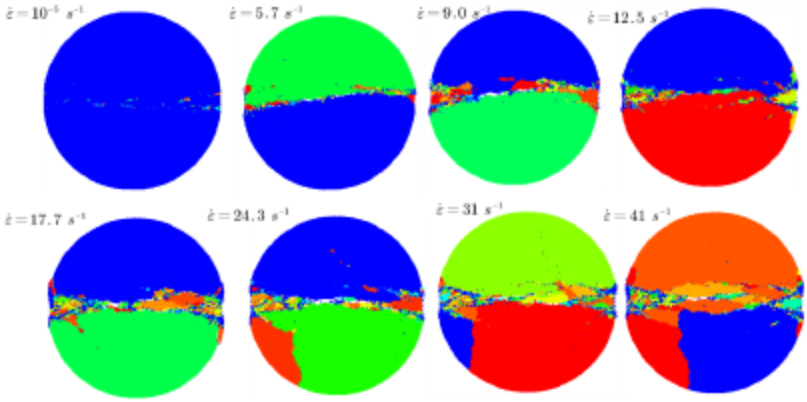

Figure. 20. The ultimate fragment states of the specimen at four strain rates.

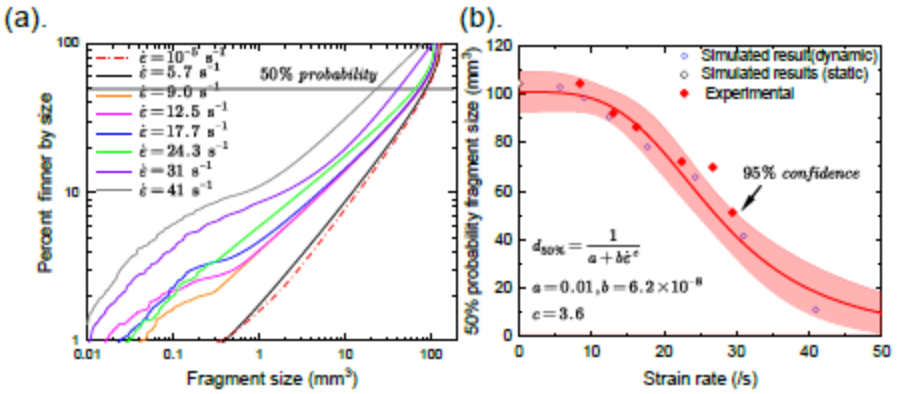

Figure. 21. (a). The cumulative distribution of fragment size at different strain rates. (b). The 50% probability fragment size change at different strain rated.

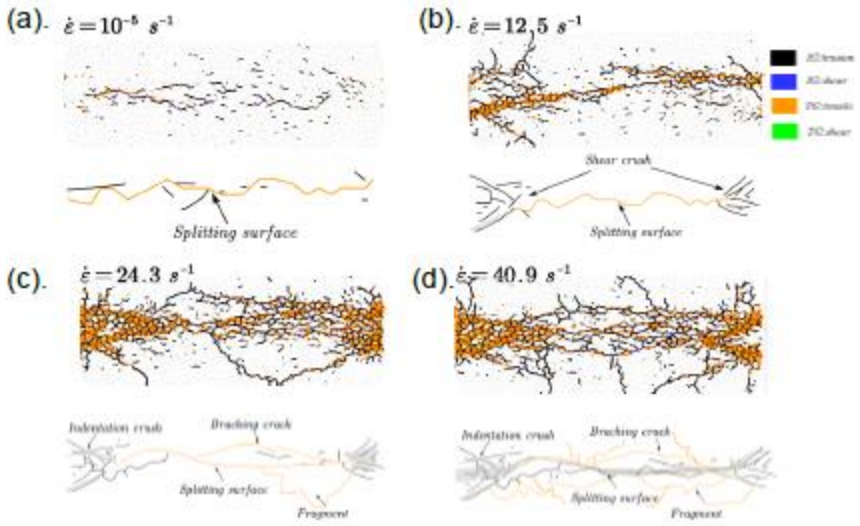

Figure. 22. The micro fracture characteristics at four different strain rates.

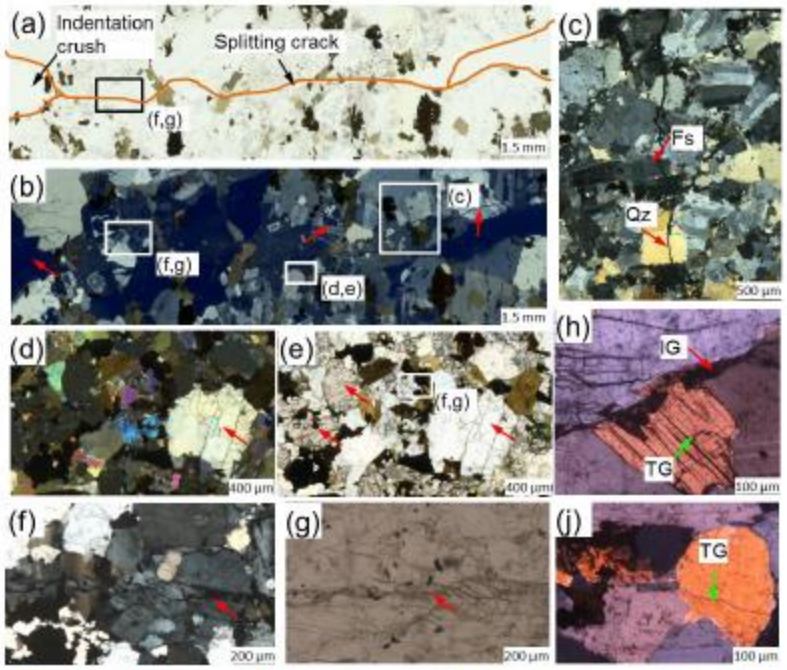

Figure. 23. Microphotographs of sample $\dot{\varepsilon}$ =14/s. (a) Plane polarized image of the whole cross section on the crack path. (b) Crossed polarized image of the same range presented in figure 23a. (c). Partial enlarged image of the splitting crack. The red arrows indicate the transgranular crack through Qs and Fs. (d,e) Plane and Crossed polarized images of the grain pulverizations, the intensive distributed cracks formed within grains. (f,g) Plane and Crossed polarized images of the shear induced cracks. (h) Partial enlarged image of transgranular shear crack and intergranular tensile crack. (j) Partial enlarged image of transgranular tensile crack.

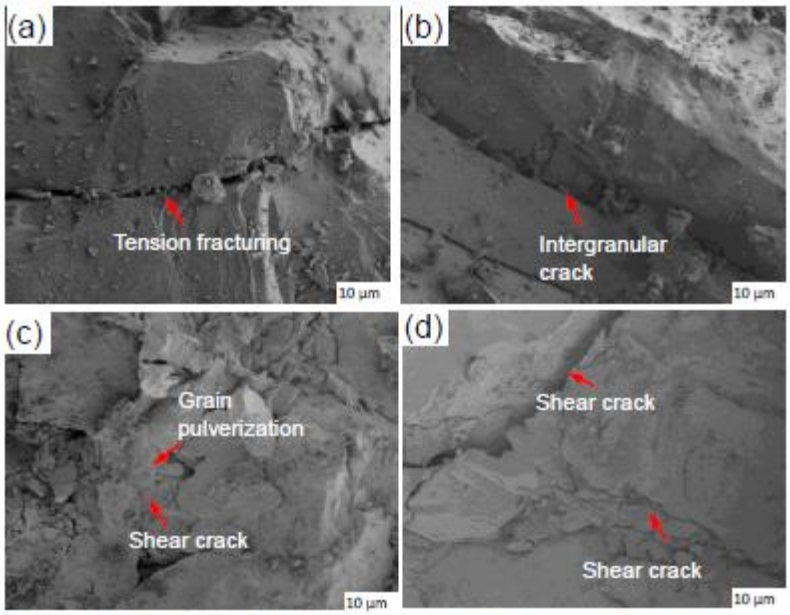

Figure. 24. Scanning electron microscope images of different mciro cracks. (a) Tension crack. (b) Intergranular crack. (c) shear induced grain pulverization. (d) Shear crack.

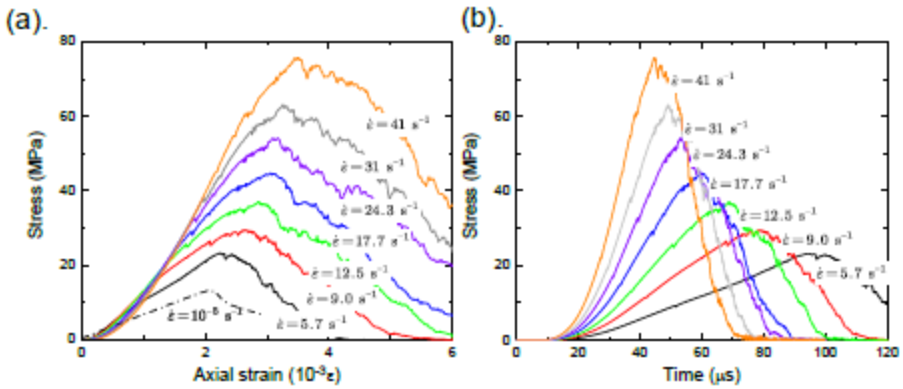

Figure. 25. The dynamic tensile stress changes at different strain rates. (a). Stress-strain curves. (b) Stress-time curves.

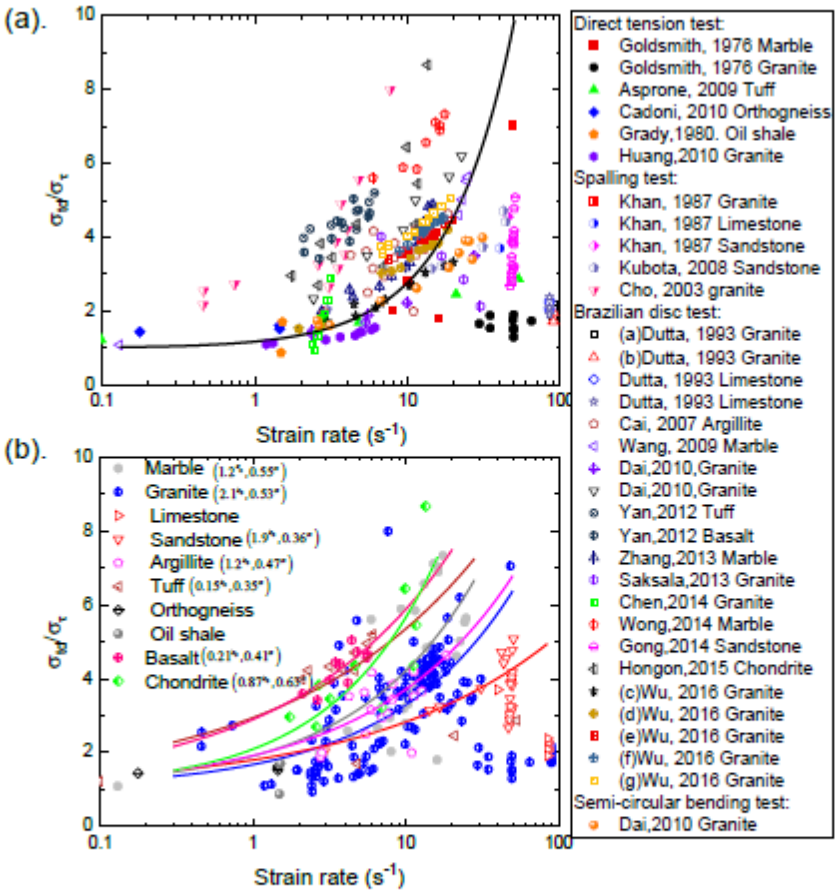

(a). Temperature T=24 °C; (b) Temperature T=-40~30 °C; (c) Confining stress σ_c=0; (d) Confining stress σ_c=5 MPa; (e) Confining stress σ_c=10 MPa; (f) Confining stress σ_c=15 MPa; (g) Confining stress σ_c=20 MPa;

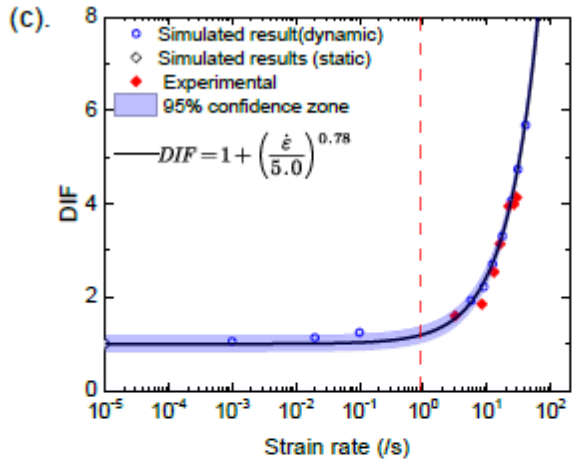

Figure. 26. A summary of the dynamic increase factor for rocks as a function of strain rates. (a) Categorized by the test methods (data from Goldsmith et al, 1976; Asprone et al,2009; Cadoni, 2010; Grady and Kipp, 1980; Huang, 2010; Khan and Irani, 1987; Cho et al, 2003; Kubota et al., 2008; Johnson, 2010; Dutta and Kim, 1993; Cai et al, 2007; Wang et al, 2009; Dai et al, 2010(a); Dai et al, 2010(b); Yan et al, 2012; Zhang and Zhao, 2013; Saksala et al, 2013; Chen et al, 2013; Wong et al, 2014; Gong and Zhao, 2014; Hogan et al, 2015; Wu et al, 2016; Dai et al, 2010). (b) Categorized by the rock types. (c) The experimental and simulated results in this study.

Table 1. The geometry information for different mineral materials.

	V_{ratio}	$d_{ave.}$ (mm)	$d_{\max.}$ (mm)	$d_{\max}/d_{\min}$
Quartz (Qz)	26.3%	1.6	3.18	3.2
Alkalifeldspar (Fs)	56.2%	2.38	6.73	5.4
Biotite (Bt)	17.5%	0.95	1.83	2.6

V_{ratio}: Volume composition; $d_{ave.}$: Average grain size; $d_{\max.}$: Maximum grain size; $d_{\max}/d_{\min}$: Ratio of maximum grain size to minimum grain size

Table .2
Micro-properties of balls and bonds of the bars

properties	Parallel bond model (mean ± std.dev.)
Ball density (kg/m^3)	9931
Ball radius (mm)	0.1
Particle-based material parameters:	
Young's modulus (E_c,GPa)	210
Stiffness ratio k_n/k_s	2.5
Bond-based material parameters:	
Young's modulus ($\overline{E}_c$,GPa)	210
Stiffness ratio $\overline{k}_n/\overline{k}_s$	2.5
Normal strength (σ,Pa)	10^{100} ± 0
Shear strength (τ,Pa)	10^{100} ± 0
Friction coefficient μ	0

Table 3. Calibrated micro parameters for different mineral materials used in GB-DEM.

	Quartz	Alkalifeldspar	Biotite	Others
General				
Volume composite V_{ratio}	27.90%	49.80%	19.60%	2.70%
Average Grain size $d_{ave.}$ (mm)	1.43	2.42	0.98	1.17
Maximum grain size $d_{\max.}$ (mm)	3.3	2.2	1	1.83
Maximum/Minimum $d_{\max}/d_{\min}$	3.2	5.4	2.6	3.7
Particle				
Minimum radius $R_{\min}$				0.08
Radius ratio $R_{\max}/R_{\min}$				1.66
Density ρ (kg/m^3)	2650	2600	3050	1650
Young Modulus E_{ball} (GPa)	95	35	32	5.8
Stiffness ratio k_n/k_s	1.0	1.8	2.0	4.0
Friction coefficient $\mu_{tra.}$	0.13	0.16	0.31	0.44
Transgranular contacts				
Young modulus $E^c_{tra.}$ (GPa)	95.0	35.0	32.0	5.8
Stiffness ratio $\overline{k}_n^{tra.}/\overline{k}_s^{tra.}$	1.0	1.8	2.0	4.0
Friction angle $\phi_{tra.}$ (degree)	7.5	9.2	17.3	23.7
Cohesion $c_{tra.}$ (MPa)	196±42	142±28	116±22	25±0
Tension $\sigma^t_{tra.}$ (MPa)	105±22	90±18	72±14	12±0
Intergranular contacts				
Parallel Young modulus $E^{pb}_{int.}$ (GPa)				0.2
Parallel stiffness ratio $\overline{k}_n^{int.}/\overline{k}_s^{int.}$				3.0
Linear Young modulus $E^c_{int.}$ (GPa)				0.2
Linear stiffness ratio $k_n^{int.}/k_s^{int.}$				1.5
Friction coefficient $\mu_{int.}$				0.8
Friction angle $\phi_{int.}$ (degree)				38.6
Cohesion $c_{int.}$ (MPa)				50.0
Tension $\sigma_t^{int.}$ (MPa)				23.0